Review of FD–TD Numerical Modeling of Electromagnetic Wave Scattering and Radar Cross Section

ALLEN TAFLOVE, SENIOR MEMBER, IEEE, AND
KORADA R. UMASHANKAR, SENIOR MEMBER, IEEE

Invited Paper

Applications of the finite-difference time-domain (FD–TD) method for numerical modeling of electromagnetic wave interactions with structures are reviewed, concentrating on scattering and radar cross section (RCS). A number of two- and three-dimensional examples of FD–TD modeling of scattering and penetration are provided. The objects modeled range in nature from simple geometric shapes to extremely complex aerospace and biological systems. Rigorous analytical or experimental validations are provided for the canonical shapes, and it is shown that FD–TD predictive data for near fields and RCS are in excellent agreement with the benchmark data. It is concluded that, with continuing advances in FD–TD modeling theory for target features relevant to the RCS problem, and with continuing advances in vector and concurrent supercomputer technology, it is likely that FD–TD numerical modeling will occupy an important place in RCS technology in the 1990s and beyond.

I. Introduction

Accurate numerical modeling of the radar cross section (RCS) of complex objects is difficult. Typical structures of interest have shapes, apertures, cavities, and material compositions or loadings which produce near fields that cannot be resolved into finite sets of modes or rays. Proper numerical modeling of such near fields requires sampling at subwavelength resolution to avoid aliasing of magnitude and phase information. The goal is to provide a self-consistent model of the mutual coupling of electrically small regions (space cells) comprising the structure.

A candidate numerical modeling approach for this purpose is the finite-difference time-domain (FD–TD) solution of Maxwell's curl equations. This approach is analogous to existing finite-difference solutions of fluid-flow problems encountered in computational aerodynamics, in that the numerical model is based on a direct solution of the governing partial differential equation. Yet FD–TD is a nontraditional approach to numerical electromagnetic modeling, where frequency-domain approaches have dominated.

FD–TD is very simple in concept and execution. Yet it is remarkably robust, providing highly accurate modeling predictions for a wide variety of electromagnetic wave interaction problems. One of the goals of this paper is to demonstrate that recent advances in FD–TD modeling concepts and software implementation, combined with advances in supercomputer technology, have expanded the scope, accuracy, and speed of FD–TD modeling to the point where it may be the preferred choice for scattering problems involving complex, electrically large, three-dimensional structures. With this in mind, this paper will succinctly review the following FD–TD modeling validations:

1) Canonical two-dimensional targets
   a) Square metal cylinder, TM polarization
   b) Circular muscle-fat-layered cylinder, TE polarization
   c) Homogeneous, anisotropic, square material cylinder, TM polarization
   d) Circular metal cylinder, conformally modeled, TE and TM polarization
   e) Flanged metal open cavity
2) Canonical three-dimensional targets
   a) Metal cube, broadside incidence
   b) Flat conducting plate, multiple monostatic RCS observations
   c) T-shaped conducting target, multiple monostatic RCS observations

The potential of FD–TD for modeling noncanonical, indeed very complex, three-dimensional objects will then be illustrated by reviewing published work which investigated the penetration of VHF and UHF plane-wave energy

Manuscript received April 12, 1988; revised October 4, 1988. This work was supported in part by the U.S. Air Force under RADC contracts F30602-79-C-0039 and F19628-82-C-0140; by NASA/Lewis under grant NAG 3-635, and by the National Science Foundation under grant ECS-8515777.

A. Taflove is with the Department of Electrical Engineering and Computer Science, Technological Institute, Northwestern University, Evanston, IL 60208, USA.

K. R. Umashankar is with the Department of Electrical Engineering and Computer Science, University of Illinois at Chicago, Chicago, IL 60680, USA.

IEEE Log Number 8927989.

0018-9219/89/0500-0682$01.00 © 1989 IEEE

into 1) the infrared seeker section of a missile and 2) the entire human body. Finally, the paper will conclude with a discussion of large-scale computer software and the potential impact of massively concurrent machines.

II. General Characteristics of FD-TD

As stated, FD-TD is a direct solution of Maxwell's time-dependent curl equations. It employs no potentials. Instead, it applies simple second-order accurate central-difference approximations [1] for the space and time derivatives of the electric and magnetic fields directly to the respective differential operators of the curl equations. This achieves a sampled-data reduction of the continuous electromagnetic field in a volume of space over a period of time. Space and time discretizations are selected to bound errors in the sampling process and to ensure numerical stability of the algorithm [2]. Electric and magnetic field components are interleaved in space to permit a natural satisfaction of tangential field continuity conditions at media interfaces. Overall, FD-TD is a marching-in-time procedure which simulates the continuous actual waves by sampled-data numerical analogs propagating in a data space stored in a computer. At each time step, the system of equations to update the field components is fully explicit, so that there is no need to set up or solve a system of linear simultaneous equations. As a consequence, the required computer storage and running time is dimensionally low, proportional only to N, where N is the number of electromagnetic field unknowns in the volume modeled.

Fig. 1(a) illustrates the time-domain wave tracking concept of the FD-TD method. A region of space (within the dashed line) is selected for field sampling in space and time. At time = 0, it is assumed that all fields within the numerical sampling region are identically zero. An incident plane wave is assumed to enter the sampling region at this time. Propagation of the incident wave is modeled by the commencement of time-stepping, which is simply the implementation of the finite-difference analog of the curl equations. Time stepping continues as the numerical analog of the incident wave strikes the modeled target embedded within the sampling region. All outgoing scattered wave analogs ideally propagate through the lattice truncation planes with negligible reflection to exit the sampling region. Phenomena such as induction of surface currents, scattering and multiple scattering, penetration through apertures, and cavity excitation are modeled time step by time step by the action of the curl equations analog. Self-consistency of these modeled phenomena is generally assured if their spatial and temporal variations are well resolved by the space and time sampling process.

Time stepping is continued until the desired late-time pulse response or steady-state behavior is achieved. An important example of the latter is the sinusoidal steady state, wherein the incident wave is assumed to have a sinusoidal dependence, and time stepping is continued until all fields in the sampling region exhibit sinusoidal repetition. This is a consequence of the limiting amplitude principle [3]. Extensive numerical experimentation with FD-TD has shown that the number of complete cycles of the incident wave required to be time stepped to achieve the sinusoidal steady state is a function of two (possibly related) factors:

1) *Target electrical size.* Numerical wave analogs must be permitted time to propagate in the FD-TD computational lattice to causally connect the physics of all regions of the target. For many targets, this requires a number of time steps sufficient to permit at least two complete front-to-back-to-front traverses of the target by a wave analog traveling at the speed of light. For example, assuming a target spanning a maximum of 10 wavelengths, it is reasonable to assume that about 40 complete cycles of the incident wave should be time-stepped (as a minimum) to achieve the sinusoidal steady state. Using a space resolution of 10 lattice cells per wavelength, this corresponds to 800 time steps.

2) *Target Q factor.* Targets having well-defined low-loss cavities or low-loss dielectric compositions may require the number of complete cycles of the incident wave to be time-stepped to approach the Q factor of the cavity resonance. Because the Q factor can be large even for electrically small or moderate size cavities, this consideration can dictate how many time steps the FD-TD code must be run to achieve the sinusoidal steady state.

Table 1 summarizes the number of sinusoidal cycles needed to achieve the steady state for a wide range of structures modeled using FD-TD over the past 15 years. In the RCS area, it has been found that target electrical size has proven to be the dominant factor. Cavities for RCS-type problems tend to be open, and therefore low Q; and the use of radar-absorbing material (RAM) serves further to reduce Q factors of structural resonances.

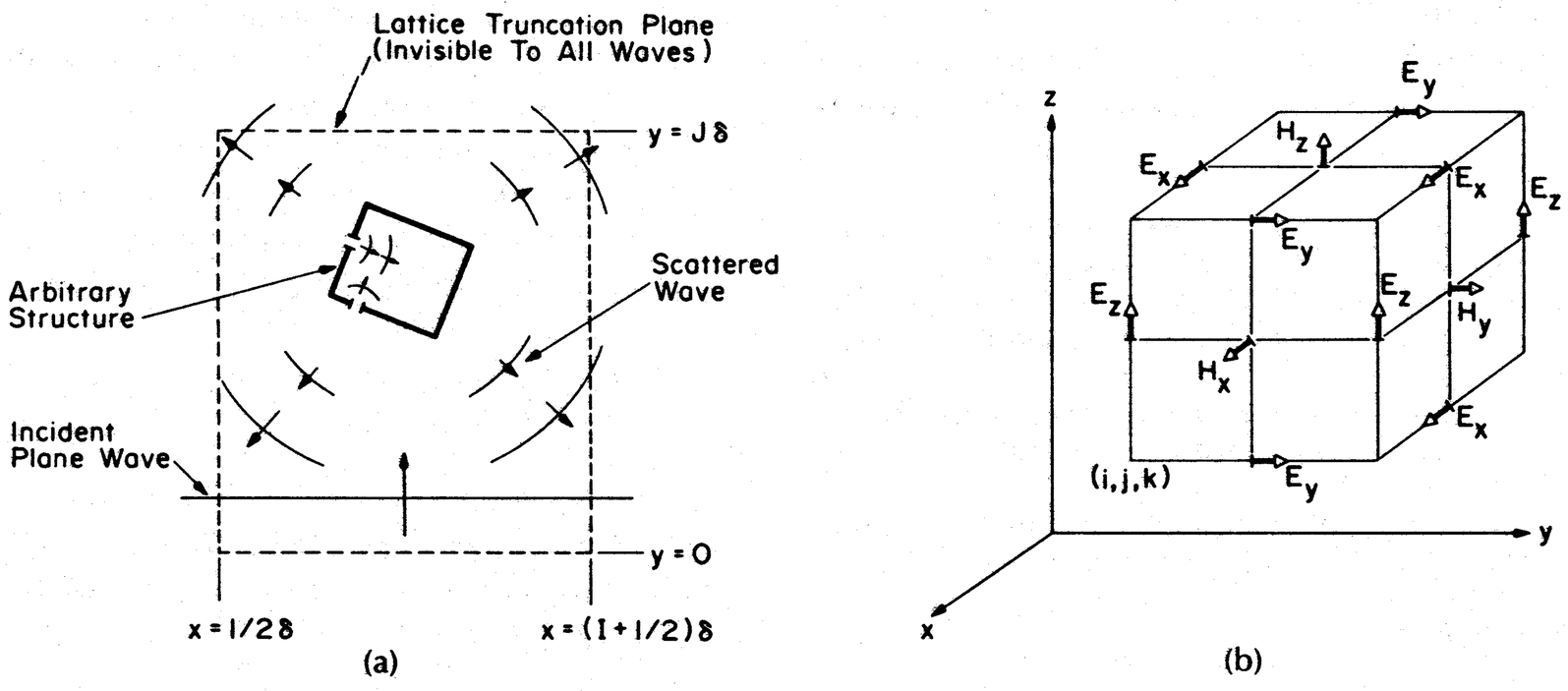

Fig. 1. Basic elements of FD-TD space lattice. (a) Time-domain wave tracking concept. (b) Lattice unit cell in Cartesian coordinates [1].

Table 1 Convergence of FD-TD to Sinusoidal Steady State

Number of Sinusoidal Cycles Needed	General Structure Type
≤5	Convex 2-D metal targets spanning less than 1 λ_0, TM case Lossy 3-D structures, especially those comprised of biological tissue media
5–20	Convex 2-D metal targets spanning 1–5 λ_0, TE case Convex 2-D dielectric targets spanning 1–5 λ_0, TM and TE cases Convex 3-D metal targets spanning 1–5 λ_0
20–40	3-D metal wires and rods spanning on the order of 1 λ_0, excited near a resonance General 3-D metal targets spanning up to 10 λ_0, including corner reflectors and open cavities
≥40	Deeply reentrant 3-D metal targets (such as engine inlets) spanning 10 λ_0 or more
≥100	3-D metal targets of arbitrary electrical size, but having aperture/cavity resonances of moderate to high Q, and excited very near such a resonance

Fig. 1(b) illustrates the positions of the electric and magnetic field components about a unit cell of the FD-TD lattice in Cartesian coordinates [1]. Note that each magnetic field vector component is surrounded by four circulating electric field vector components, and vice versa. This arrangement permits not only a centered-difference analog to the space derivatives of the curl equations, but also a natural geometry for implementing the integral form of Faraday's law and Ampère's law at the space-cell level. This integral interpretation permits a simple but effective modeling of the physics of smoothly curved target surfaces, as will be seen later.

Fig. 2 illustrates how an arbitrary three-dimensional scatterer is embedded in an FD-TD space lattice comprised of the unit cells of Fig. 1(b). Simply, the desired values of electrical permittivity and conductivity are assigned to each electric field component of the lattice. Correspondingly, desired values of magnetic permeability and equivalent conductivity are assigned to each magnetic field component of the lattice. The media parameters are interpreted by the FD-TD program as local coefficients for the time-stepping algorithm. Specification of media properties in this component-by-component manner results in a stepped-edge, or staircase, approximation of curved surfaces. Continuity of tangential fields is assured at the interface of dissimilar media with this procedure. There is no need for special field matching at media interface points. Stepped-edge approximation of curved surfaces has been found to be adequate in the FD-TD modeling problems studied in the 1970s and early 1980s, including wave interactions with biological tissues [4], penetration into cavities [5]–[7], and electromagnetic pulse (EMP) interactions with complex structures [8]–[10]. However, recent interest in wide-dynamic-range models of scattering by curved targets has prompted the development of surface-conforming FD-TD approaches which eliminate staircasing. These are summarized in a later section.

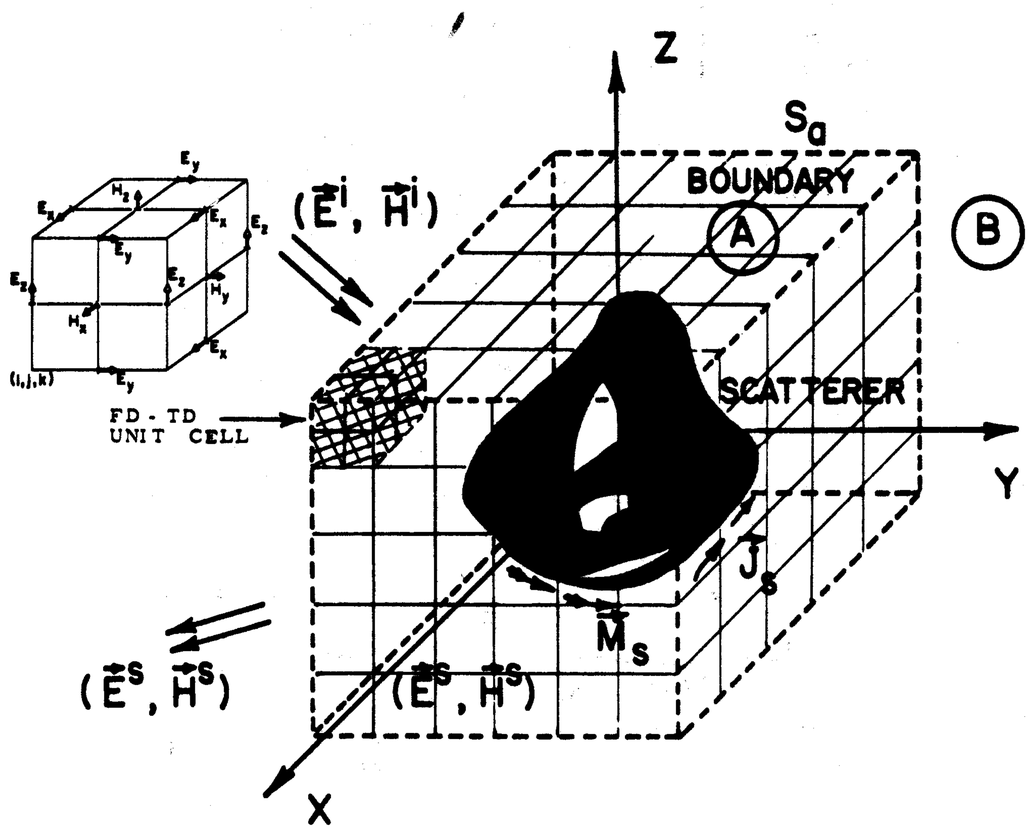

Fig. 2. Arbitrary three-dimensional scatterer embedded in FD-TD space lattice.

III. Review of FD-TD Algorithm Details

Table 2 lists the six coupled equations for the electric and magnetic fields which comprise Maxwell's equations in Cartesian coordinates. Table 3 lists the assumed space-time

Table 2 Maxwell's Curl Equations in Cartesian Coordinates

$$\frac{\partial H_x}{\partial t} = \frac{1}{\mu}\left(\frac{\partial E_y}{\partial z} - \frac{\partial E_z}{\partial y} - \rho' H_x\right) \tag{1a}$$

$$\frac{\partial H_y}{\partial t} = \frac{1}{\mu}\left(\frac{\partial E_z}{\partial x} - \frac{\partial E_x}{\partial z} - \rho' H_y\right) \tag{1b}$$

$$\frac{\partial H_z}{\partial t} = \frac{1}{\mu}\left(\frac{\partial E_x}{\partial y} - \frac{\partial E_y}{\partial x} - \rho' H_z\right) \tag{1c}$$

$$\frac{\partial E_x}{\partial t} = \frac{1}{\epsilon}\left(\frac{\partial H_z}{\partial y} - \frac{\partial H_y}{\partial z} - \sigma E_x\right) \tag{1d}$$

$$\frac{\partial E_y}{\partial t} = \frac{1}{\epsilon}\left(\frac{\partial H_x}{\partial z} - \frac{\partial H_z}{\partial x} - \sigma E_y\right) \tag{1e}$$

$$\frac{\partial E_z}{\partial t} = \frac{1}{\epsilon}\left(\frac{\partial H_y}{\partial x} - \frac{\partial H_x}{\partial y} - \sigma E_z\right) \tag{1f}$$

where

E_x, E_y, E_z = Cartesian components of electric field, volts/meter
H_x, H_y, H_z = Cartesian components of magnetic field, amperes/meter
ϵ = electric permittivity, farads/meter
σ = electric conductivity, siemens/meter
μ = magnetic permeability, henrys/meter
ρ' = equivalent magnetic loss, ohms/meter

Table 3 Central-Difference Approximations to Space and Time Partial Derivatives

$$(i, j, k) = (i\Delta x, j\Delta y, k\Delta z) \tag{2a}$$

$$F^n(i, j, k) = F(i\Delta x, j\Delta y, k\Delta z, n\Delta t) \tag{2b}$$

$$\frac{\partial F^n(i, j, k)}{\partial x} = \frac{F^n(i + \frac{1}{2}, j, k) - F^n(i - \frac{1}{2}, j, k)}{\Delta x} + \text{order } (\Delta x^2) \tag{3a}$$

$$\frac{\partial F^n(i, j, k)}{\partial t} = \frac{F^{n+1/2}(i, j, k) - F^{n-1/2}(i, j, k)}{\Delta t} + \text{order } (\Delta t^2) \tag{3b}$$

For a cubic space lattice, $\Delta x = \Delta y = \Delta z \equiv \delta$.

Table 4 Examples of Finite-Difference Expressions to Time-Step Field Vector Components

$$H_x^{n+1/2}(i, j+\tfrac{1}{2}, k+\tfrac{1}{2}) = \frac{1 - \dfrac{\rho'(i, j+\frac{1}{2}, k+\frac{1}{2})\Delta t}{2\mu(i, j+\frac{1}{2}, k+\frac{1}{2})}}{1 + \dfrac{\rho'(i, j+\frac{1}{2}, k+\frac{1}{2})\Delta t}{2\mu(i, j+\frac{1}{2}, k+\frac{1}{2})}} \cdot H_x^{n-1/2}(i, j+\tfrac{1}{2}, k+\tfrac{1}{2})$$

$$+ \frac{\Delta t}{\mu(i, j+\frac{1}{2}, k+\frac{1}{2})} \cdot \frac{1}{1 + \dfrac{\rho'(i, j+\frac{1}{2}, k+\frac{1}{2})\Delta t}{2\mu(i, j+\frac{1}{2}, k+\frac{1}{2})}}$$

$$\cdot \left[\frac{E_y^n(i, j+\frac{1}{2}, k+1) - E_y^n(i, j+\frac{1}{2}, k)}{\Delta z} \right.$$

$$\left. + \frac{E_z^n(i, j, k+\frac{1}{2}) - E_z^n(i, j+1, k+\frac{1}{2})}{\Delta y} \right] \tag{4a}$$

$$E_z^{n+1}(i, j, k+\tfrac{1}{2}) = \frac{1 - \dfrac{\sigma(i, j, k+\frac{1}{2})\Delta t}{2\epsilon(i, j, k+\frac{1}{2})}}{1 + \dfrac{\sigma(i, j, k+\frac{1}{2})\Delta t}{2\epsilon(i, j, k+\frac{1}{2})}} \cdot E_z^n(i, j, k+\tfrac{1}{2})$$

$$+ \frac{\Delta t}{\epsilon(i, j, k+\frac{1}{2})} \cdot \frac{1}{1 + \dfrac{\sigma(i, j, k+\frac{1}{2})\Delta t}{2\epsilon(i, j, k+\frac{1}{2})}}$$

$$\cdot \left[\frac{H_y^{n+1/2}(i+\frac{1}{2}, j, k+\frac{1}{2}) - H_y^{n+1/2}(i-\frac{1}{2}, j, k+\frac{1}{2})}{\Delta x} \right.$$

$$\left. + \frac{H_x^{n+1/2}(i, j-\frac{1}{2}, k+\frac{1}{2}) - H_x^{n+1/2}(i, j+\frac{1}{2}, k+\frac{1}{2})}{\Delta y} \right] \tag{4b}$$

notation for the field vector components sampled at discrete lattice locations and at discrete time steps. This table also provides the central-difference approximations to the space and time partial derivatives of Maxwell's equations, using the assumed sampled-field notation. Finally, Table 4 provides example finite-difference time-stepping expressions for a magnetic and an electric field component. As noted earlier, all quantities on the right-hand side of each time-stepping expression are known (stored in computer memory), so that the expressions are fully explicit.

The choice of δ and Δt is motivated by reasons of accuracy and algorithm stability, respectively. To ensure the accuracy of the computed spatial derivatives of the electromagnetic fields, δ must be small compared to a wavelength. $\delta \leq \lambda/10$ is sufficient to realize less than $\pm 7\%$ uncertainty (± 0.6 dB) of the FD-TD solution of near fields due to the approximation of the spatial derivatives [5]. For $\delta \leq \lambda/20$, this uncertainty drops to less than $\pm 2\%$ (± 0.2 dB). δ should also be small enough to permit resolution of the principal surfaces or volumetric details of the structure modeled.

To ensure the stability of the time-stepping algorithm exemplified by (4a) and (4b), Δt is chosen to satisfy the inequality [2]

$$\Delta t \leq \left(\frac{1}{\Delta x^2} + \frac{1}{\Delta y^2} + \frac{1}{\Delta z^2} \right)^{-1/2} c_{\max}^{-1}$$

$$\leq \frac{\delta}{c_{\max}\sqrt{3}} \quad \text{for a cubic lattice} \tag{5}$$

where c_{max} is the maximum wave phase velocity within the model. Note that the corresponding stability criterion set forth in [1, eqs. (7) and (8)] is incorrect, as shown in [2].

Fig. 3(a) illustrates the division of the FD-TD lattice into total-field and scattered-field regions. This division has been found to be very useful since it permits the efficient sim-

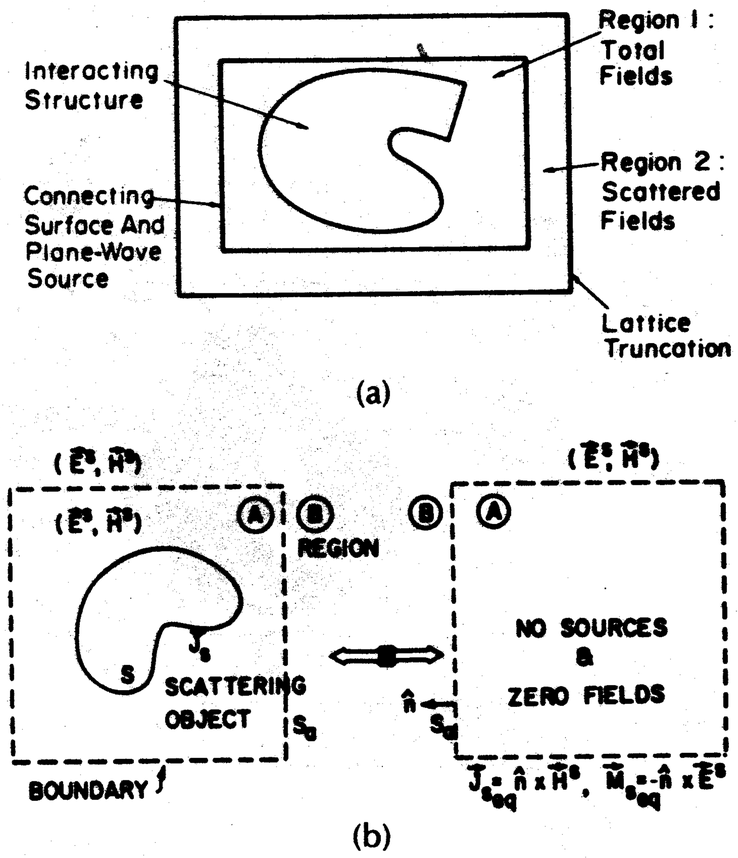

Fig. 3. Zoning of FD-TD space lattice. (a) Total-field and scattered-field regions [11], [12]. (b) Near-field to far-field integration surface located in the scattered-field region [12].

ulation of an incident plane wave in the total-field region with arbitrary angle of incidence, polarization, time-domain waveform, and duration [11], [12]. Three additional important benefits arise from this lattice division as follows.

1) *Large near-field computational dynamic range.* Because the target of interest is embedded in the total-field region, low total-field levels in shadow regions or within shielding enclosures are computed directly without suffering subtraction noise (as would be the case if scattered fields in such regions were time-stepped, and then added to a canceling incident field to obtain the low total-field levels). Avoidance of subtraction noise is the key to obtaining near-field computational dynamic ranges exceeding 60 dB [5].

2) *Natural satisfaction of electromagnetic boundary conditions.* Embedding the target in the total-field region permits a natural satisfaction of tangential field continuity across media interfaces, as discussed earlier, without having to compute the incident field at possibly thousands or tens of thousands of points along complicated media-interface loci that are unique to each target. The zoning arrangement of Fig. 3(a) requires computation of the incident field only along the rectangular connecting surface between total-field and scattered-field regions. This surface is fixed, that is, independent of the shape or composition of the enclosed target being modeled. A substantial benefit in computer running time arises as a result, a benefit that increases as the complexity of the target increases.

3) *Systematic computation of bistatic RCS.* The provision of a well-defined scattered-field region in the FD-TD lattice permits the near-field to far-field transformation illustrated in Fig. 3(b). The dashed virtual surface (field observation locus) shown in Fig. 3(b) can be located along convenient lattice planes in the scattered-field region of Fig. 3(a). Tangential scattered E and H fields computed via FD-TD at this virtual surface can then be weighted by the free-space Green's function and then integrated (summed) to provide the far-field response and RCS (full bistatic response for the assumed illumination angle) [12]–[14]. The near-field integration surface has a fixed rectangular shape and thus is independent of the shape or composition of the enclosed target being modeled.

Fig. 3(a) uses the term "lattice truncation" to designate the outermost lattice planes in the scattered-field region. The fields at these planes cannot be computed using the centered-differencing approach discussed earlier because of the assumed absence of known field data at points outside of the lattice truncation. These data are needed to form the central differences. Therefore, an auxiliary lattice truncation condition is necessary. This condition must be consistent with Maxwell's equations in that an outgoing scattered-wave numerical analog striking the lattice truncation must exit the lattice without appreciable nonphysical reflection, just as if the lattice truncation was invisible.

It has been shown that the required lattice truncation condition is really a radiation condition in the near field [15]–[17]. A very successful second-order accurate finite-difference approximation of the exact radiation condition in Cartesian coordinates was introduced in [11]. This approximation was subsequently used in a variety of two- and three-dimensional FD-TD scattering codes [12]–[14], yielding excellent results for both near and far fields. (For example, all FD-TD results in this paper, with the exception of the missile seeker model of Section VI, were obtained using these codes.) However, recent interest in wide-dynamic-range models of scattering has prompted research in the construction of even more accurate near-field radiation conditions, including fixed third-order approximations [18], [19], adaptive conditions [20], and predictor–corrector conditions [21]. The goal here is to reduce the numerical lattice noise due to nonphysical reflections of wave analogs at the lattice truncations by at least one order of magnitude (20 dB) relative to that achieved by the second-order condition of [11].

IV. FD-TD Modeling Validations for Canonical Two-Dimensional Targets

Analytical and code-to-code validations have been obtained relative to FD-TD modeling of a wide variety of canonical two-dimensional targets. Both convex and reentrant (cavity-type) shapes have been studied. Further, target material compositions have included perfect conductors, homogeneous and inhomogeneous lossy dielectrics, and anisotropic dielectric and permeable media. Selected validations will be reviewed here.

A. Square Metal Cylinder, TM Polarization [12]

Here we consider the scattering of a TM-polarized plane wave obliquely incident upon a square metal cylinder of electrical size $k_0 s = 2$, where s is the side width of the cylinder. The FD-TD grid employs square unit cells of size $s/20$, and the grid truncation (radiation boundary) is located at a uniform distance of 20 cells from the cylinder surface.

Fig. 4 compares the magnitude and phase of the cylinder surface electric current distribution computed using FD-TD to that computed using a benchmark frequency-domain electric-field integral equation (EFIE) method-of-moments (MoM) code. The MoM code assumes target symmetry and discretizes one-half of the cylinder surface with 84 divisions. The FD-TD computed surface current is taken as $\hat{n} \times \vec{H}_{\tan}$, where $\hat{n}$ is the unit normal vector at the cylinder surface and $\vec{H}_{\tan}$ is the FD-TD value of the magnetic field vector component in free space immediately adjacent to the cylinder surface. From Fig. 4 we see that the magnitude of the FD-TD computed surface current agrees with the MoM solution to better than $\pm 1\%$ (± 0.09 dB) at all comparison points more than 2 FD-TD space cells from the cylinder corners (current singularities). The phase of the FD-TD solution agrees with the MoM solution to within $\pm 3°$ at virtually every comparison point, including the shadow region.

B. Circular Muscle-Fat-Layered Cylinder, TE Polarization [22]

Here we consider the penetration of a TE-polarized plane wave into a 15-cm-radius muscle-fat-layered cylinder. The inner layer (radius 7.9 cm) is assumed to be comprised of muscle having a relative permittivity of 72 and a conductivity of 0.9 S/m. The outer layer is assumed to be comprised of fat having a relative permittivity of 7.5 and a conductivity of 0.048 S/m. An illumination frequency of 100 MHz is modeled, with the FD-TD grid cell size set equal to 1.5 cm (approximately 1/24 wavelength within the muscle). A

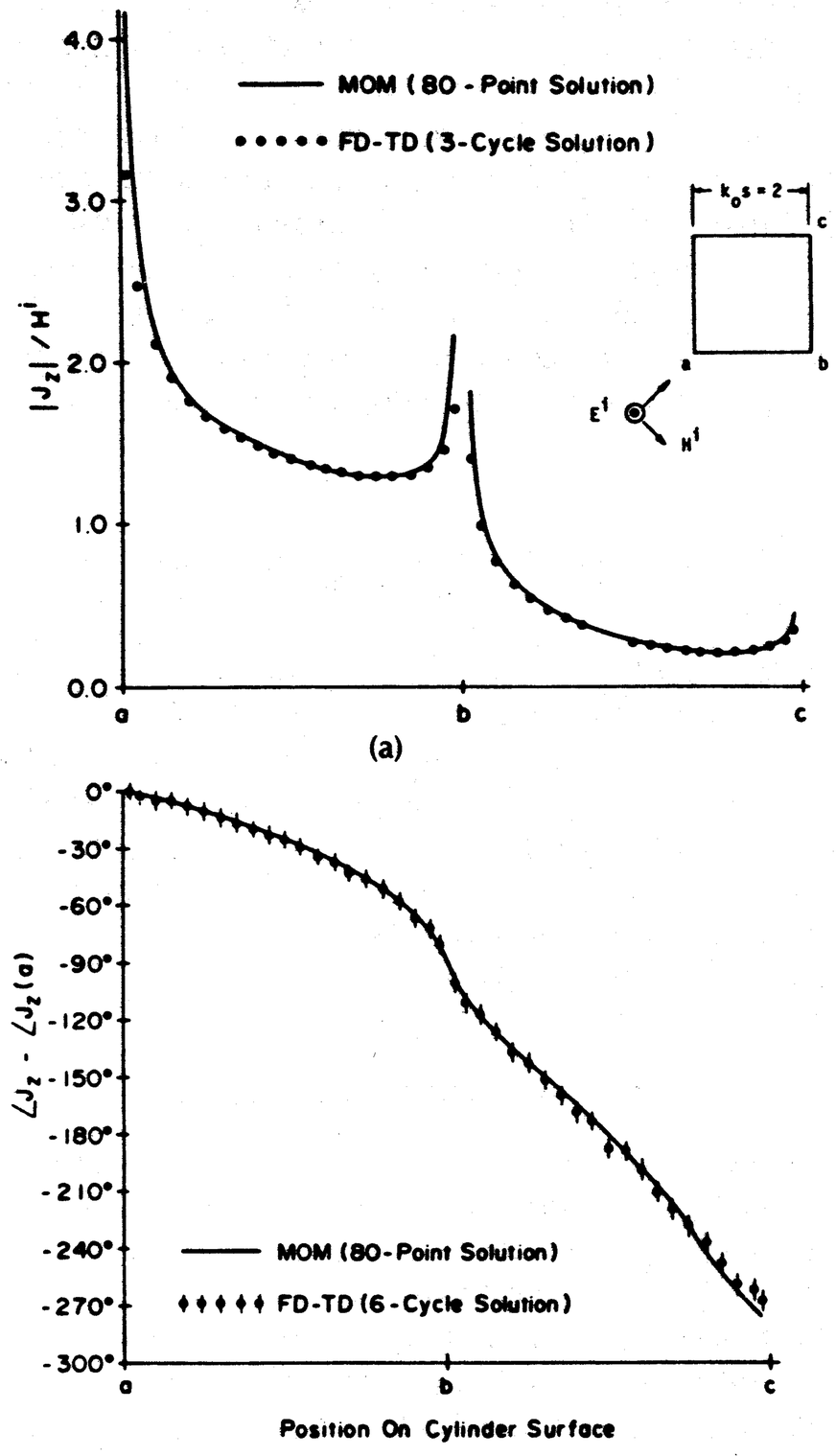

Fig. 4. Comparison of FD-TD and EFIE-MoM results for longitudinal surface electric current distribution induced on a perfectly conducting square cylinder of size $k_0 s = 2$. (a) Magnitude. (b) Phase [12].

stepped-edge (staircase) approximation of the circular layer boundaries is used.

Fig. 5, taken from [22], shows the analytical validation results for the magnitude of the penetrating electric field vector components along two cuts through the muscle-fat cylinder, one parallel to the direction of propagation of the incident wave, and one parallel to the incident electric field vector. The exact solution is obtained by summing sufficient terms of the eigenfunction expansion to assure convergence of the sum. Excellent agreement of the FD-TD and exact solutions is noted, even at jump discontinuities of the field or the slope of the field distribution that occur at the layer boundaries. This fine agreement is observed *despite the stepped-edge approximation* of the circular layer boundaries.

C. Homogeneous, Anisotropic, Square Material Cylinder, TM Polarization [23]

The ability to independently specify electrical permittivity and conductivity for each *E* vector component in the FD-TD lattice, and magnetic permeability and equivalent conductivity for each *H* vector component, leads immediately to the possibility of using FD-TD to model material targets having diagonal-tensor electric and magnetic properties. No alteration of the basic FD-TD algorithm is required. The more complicated behavior associated with off-diagonal tensor components can also be modeled, in principle, with some algorithm complications [24].

Recent development of analytical and numerical treatment of coupled surface combined-field integral equations (CFIE) for modeling scattering by arbitrarily shaped two-dimensional anisotropic targets [23] has permitted detailed tests of the accuracy of FD-TD anisotropic models. Fig. 6 illustrates the results of one such test. Here the magnitude of the equivalent surface electric current induced by TM illumination of a square anisotropic cylinder is graphed as a function of position along the cylinder surface for both

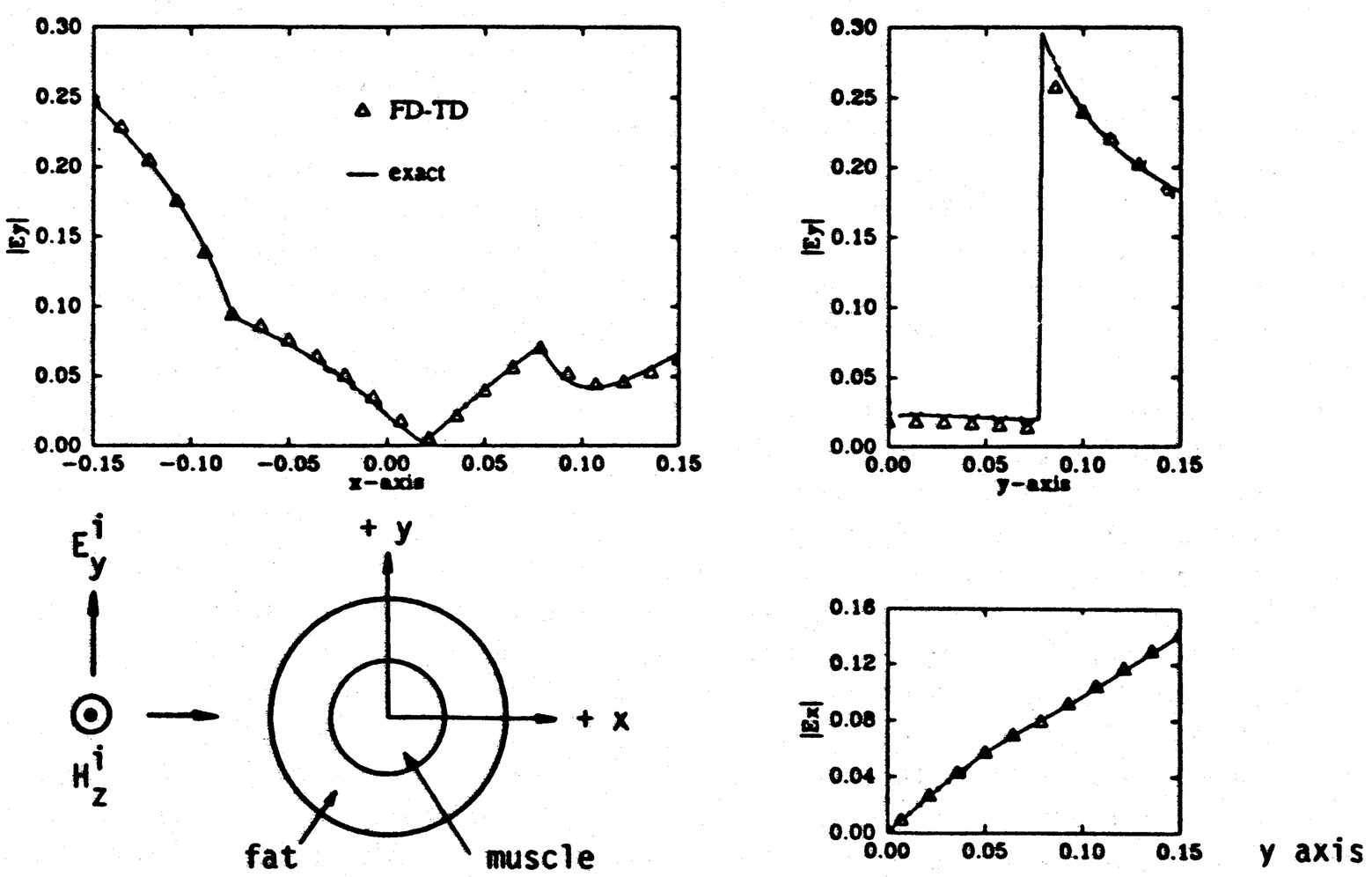

Fig. 5. Comparison of FD-TD and exact summed-eigenfunction solutions for distributions of penetrating electric field vector components within a circular muscle-fat-layered cylinder, TE polarization case at 100 MHz [22].

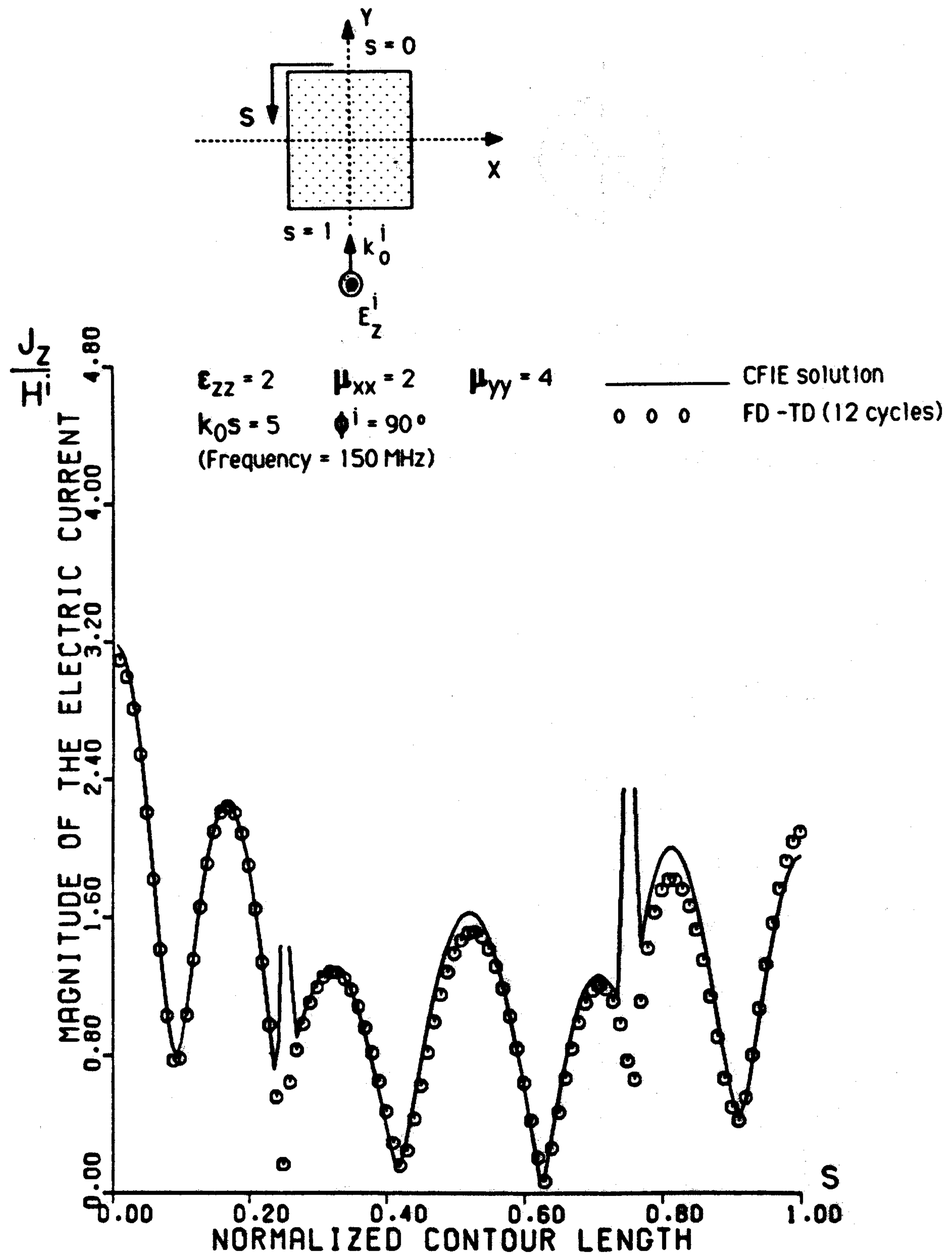

Fig. 6. Comparison of FD-TD and CFIE-MoM results for longitudinal surface electric current distribution induced on an anisotropic dielectric-permeable square cylinder of size $k_0 s = 5$, TM case [23].

the FD-TD and the CFIE MoM models. The incident wave propagates in the $+y$ direction and has a $+z$-directed electric field. The square cylinder has an electrical size $k_0 s = 5$, permittivity $\epsilon_{zz} = 2$, and diagonal permeability tensor $\mu_{xx} = 2$ and $\mu_{yy} = 4$. For the test shown, the FD-TD grid cell size is set equal to $s/50$, and the radiation boundary is located at a uniform distance of 20 cells from the cylinder surface.

From Fig. 6 we see that the FD-TD and CFIE results agree very well almost everywhere on the cylinder surface, despite the presence of a complicated series of peaks and nulls. Disagreement is noted at the cylinder corners where CFIE predicts sharp local peaks, but FD-TD predicts local nulls. Studies are continuing to resolve this corner physics issue.

D. Circular Metal Cylinder, TE and TM Polarization

A significant flaw in previous FD-TD models of conducting structures with smooth curved surfaces has been the need to use stepped-edge (staircase) approximations of the actual structure surface. Although not a serious problem for modeling wave penetration and scattering for low-Q metal cavities, recent FD-TD studies have shown that stepped approximations of curved walls and aperture surfaces can shift center frequencies of resonant responses by 1-2% for Q factors of 30 to 80, and can possibly introduce spurious nulls [25]. In the area of scattering by convex shapes, the use of stepped-surface approximations has limited application of FD-TD in modeling the important class of targets where surface roughness, exact curvature, and dielectric or permeable loading are important factors in determining the radar cross section.

Recently three different types of FD-TD conformal surface models have been proposed and examined for scattering problems:

1) *Locally distorted grid models.* These preserve the basic Cartesian grid arrangement of field components at all space cells except those immediately adjacent to the target surface. Space cells adjacent to the target surface are deformed to conform with the surface locus. Slightly modified time-stepping expressions for the field components in these cells are obtained by applying either a modified finite-volume technique [26] or the integral form of Faraday's law and Ampère's law about the perimeters of the deformed space cells [27].

2) *Globally distorted grid models, body fitted.* These employ available numerical mesh generation schemes to construct non-Cartesian grids which are continuously and globally stretched to conform with smoothly shaped targets. In effect, the Cartesian grid is mapped to a numerically generated coordinate system wherein the target surface contour occupies a locus of constant equivalent "radius." Time-stepping expressions are adapted either from the Cartesian FD-TD case [28] or from a characteristics-based method used in computational fluid dynamics [29].

3) *Globally distorted grid models, unstructured.* These employ available mesh generation schemes to construct non-Cartesian grids comprised of an unstructured array of space-filling cells. Target surface features are appropriately fit into the unstructured grid, with local grid resolution and cell shape selected to provide the desired geometric modeling aspects. An example of this class is the control-region approach discussed in [30].

Research is ongoing for each of these types of conformal surface models. Key questions concerning the usefulness of each model include the following:

1) Computer resources involved in mesh generation
2) Severity of numerical artifacts introduced by grid distortion, including numerical instability, dispersion, nonphysical wave reflection, and subtraction noise limitation of near-field computational dynamic range
3) Comparative computer resources for running the actual RCS models, especially for three-dimensional targets spanning more than 10 wavelengths

The accuracy of locally distorted grid models using the integral form of Faraday's law applied around the perimeters of the deformed space cells adjacent to a smoothly curved target is illustrated in Fig. 7 for TE and TM illumination cases. Here a moderate-resolution Cartesian FD-TD grid (having 1/20 wavelength cell size) is used to compute the azimuthal or longitudinal current distribution on the surface of a $ka = 5$ circular metal cylinder. For both polarizations it is seen that the conformal FD-TD model achieves an accuracy of 1.5% or better at most surface points relative to the exact series solution. Computer running time for the conformal FD-TD model is essentially the same as for the old staircase FD-TD model since only a few H components immediately adjacent to the target surface require a slightly modified time-stepping relation.

E. Flanged Metal Open Cavity [20], [31]

Here we consider the interaction of a TM-polarized plane wave obliquely incident upon a flanged metal open cavity.

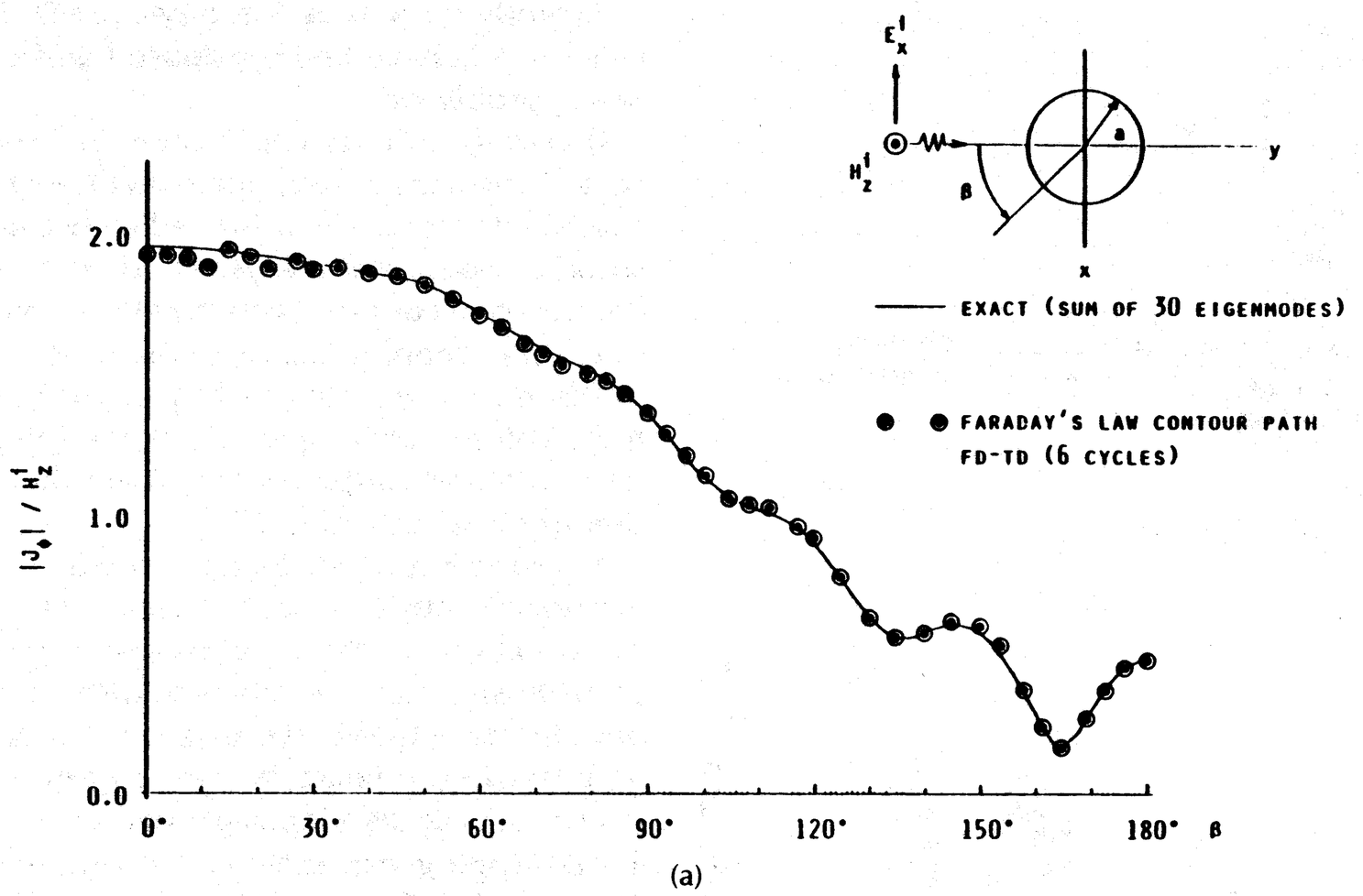

(a)

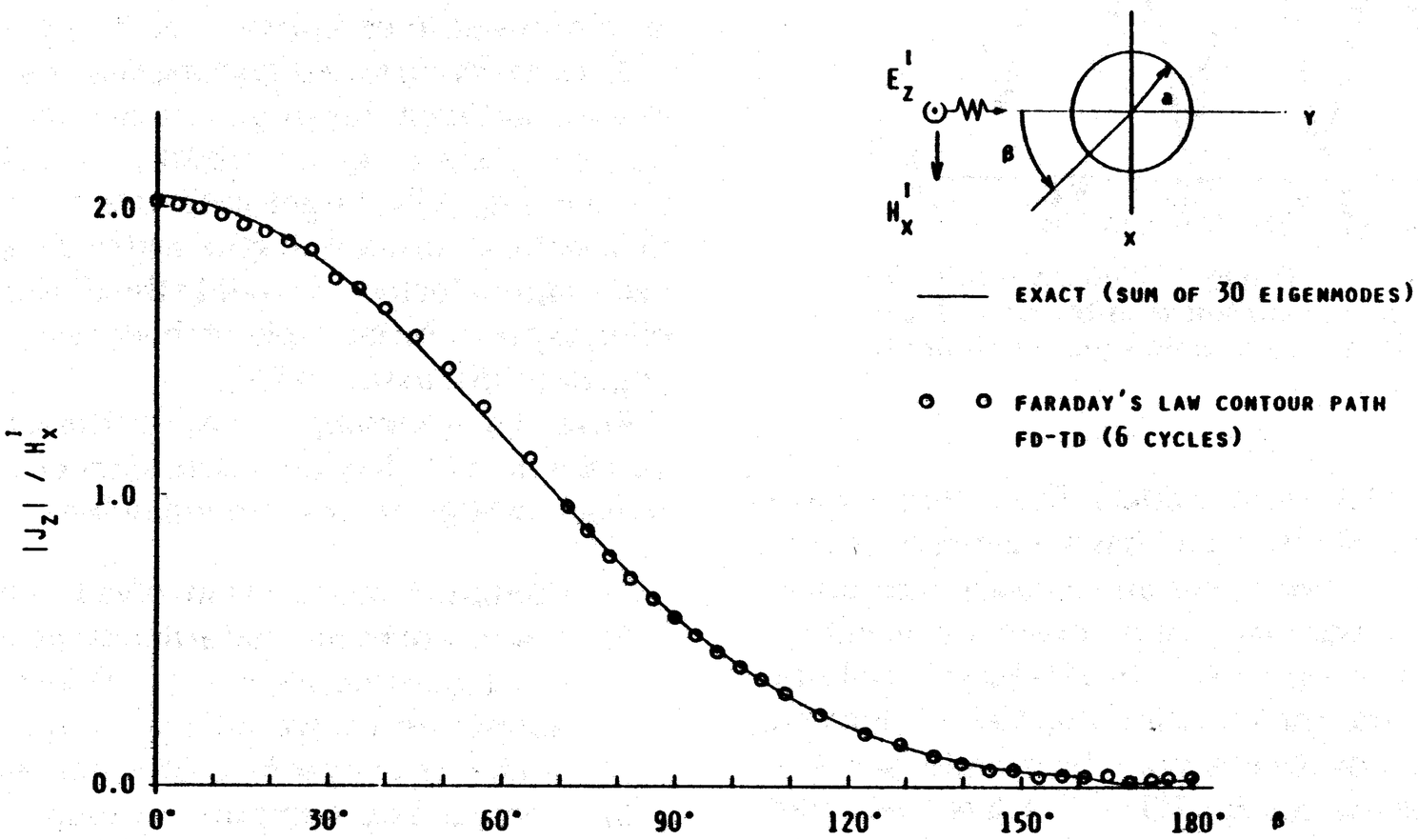

(b)

Fig. 7. Comparison of FD-TD and exact summed-eigenfunction solutions for surface electric current distribution induced on a $k_0a = 5$ circular conducting cylinder (conformal FD-TD model used, 0.05 wavelength grid cell size). (a) TE case, azimuthal current. (b) TM case, longitudinal current [27].

The open cavity is formed by a flanged parallel-plate waveguide having a plate spacing $a = 1$ m, short-circuited by a metal plate located at a distance $d = 1$ m from the aperture. At the assumed illumination frequency of 382 MHz, $ka = kd = 8$, and only the first two TE waveguide modes propagate within the open cavity. An oblique angle of incidence $\alpha = 30°$ is assumed for this case.

Fig. 8 compares the magnitude and phase of the penetrating electric field within the cavity 2/3 m from the aperture computed using FD-TD to that obtained analytically using a cavity modal expansion and on-surface radiation condition (OSRC) theory [31]. Good agreement is seen.[1] Fig. 9 shows a similar comparison for the bistatic RCS pattern due to the induced aperture field distribution. Again, good agreement is noted.

[1]It should be noted that the results obtained using the cavity modal expansion and OSRC represent a good approximation, but not a rigorous solution.

V. FD-TD Modeling Validations for Canonical Three-Dimensional Targets

Analytical, code-to-code, and experimental validations have been obtained relative to FD-TD modeling of a wide variety of canonical three-dimensional structures, including cubes, flat plates, corner reflectors, and aperture-perforated cavities. Selected validations will be reviewed here.

A. Metal Cube, Broadside Incidence [13]

Results are now shown for the FD-TD computed surface electric current distribution on a metal cube subject to

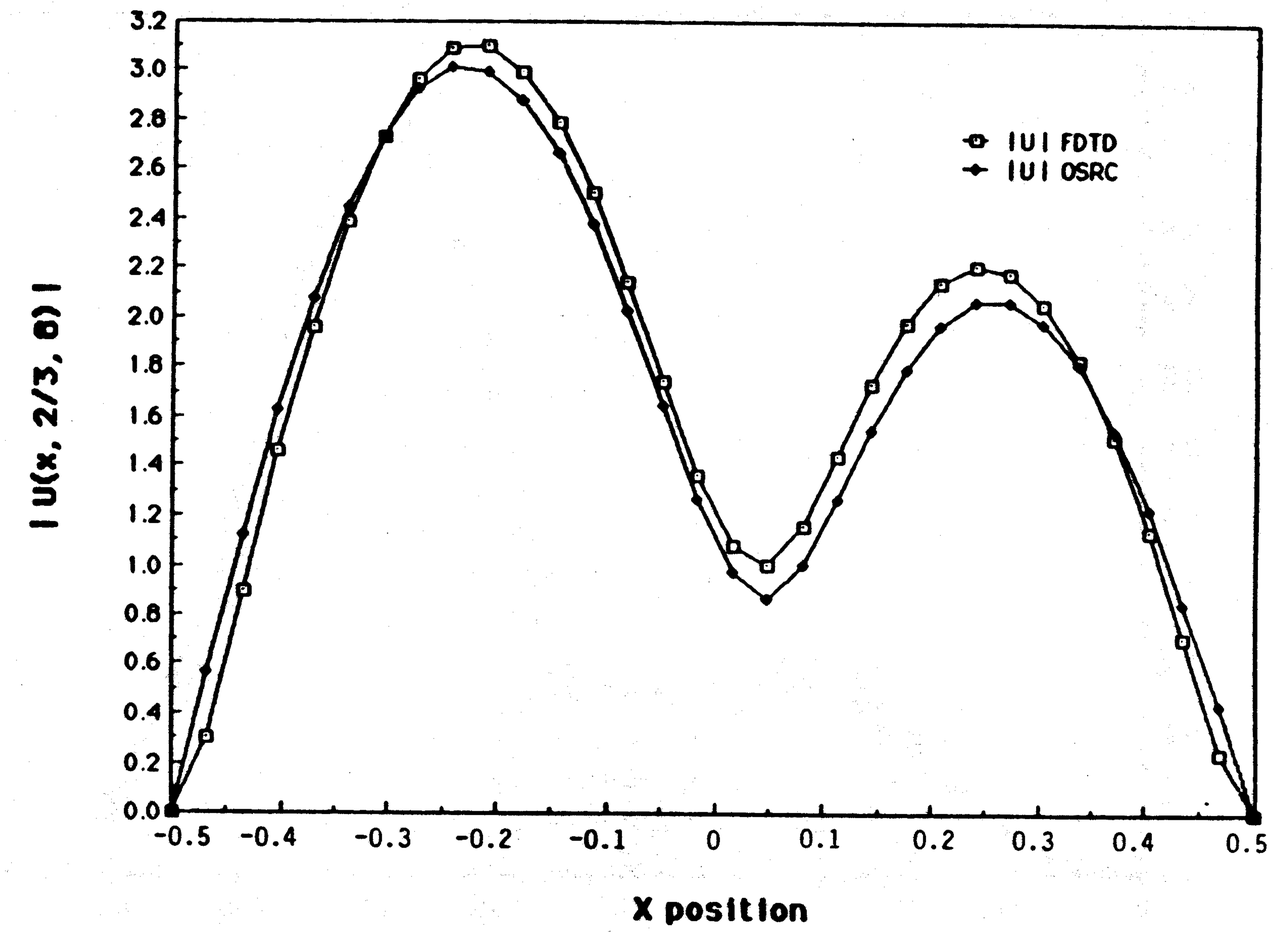

Fig. 8. Comparison of FD-TD and modal/OSRC approximate solution for penetrating electric field distribution 2/3 m within flanged open cavity. (a) Magnitude. (b) Phase [20], [31].

plane-wave illumination at broadside incidence. The electric current distribution is compared to that computed by a standard frequency-domain MoM code which discretizes target surfaces using triangular patches. It is shown that a very high degree of correspondence exists between the two sets of predictive data.

The detailed surface current study involves a cube of electrical size $k_0 s = 2$, where s is the side width of the cube. For the FD-TD model, each face of the cube is spanned by 20×20 space cells, and the radiation boundary is located at a uniform distance of 15 cells from the cube surface. For the MoM model, each face of the cube is spanned by either 18 or 32 triangular patches to test the convergence of the MoM model. Comparative results for surface current are graphed along two straight-line loci along the cube: $\overline{abcd}$, which is in the plane of the incident magnetic field, and $\overline{ab'c'd}$, which is in the plane of the incident electric field.

Fig. 10 compares the FD-TD and MoM results for the magnitude and phase of the "looping" current along $\overline{ab'c'd}$. The FD-TD values agree with the high-resolution MoM data to better than $\pm 2.5\%$ (± 0.2 dB) at all comparison points. Phase agreement for the same sets of data is better than $\pm 1°$. (The low-resolution MoM data have a phase anomaly in the shadow region.) In Fig. 11, comparably excellent agreement is obtained for the z-directed current along $\overline{abcd}$, but only after incorporation of an a priori edge-correction term in the MoM code [32] to enable it to properly model the current singularities at the cube corners b and c.

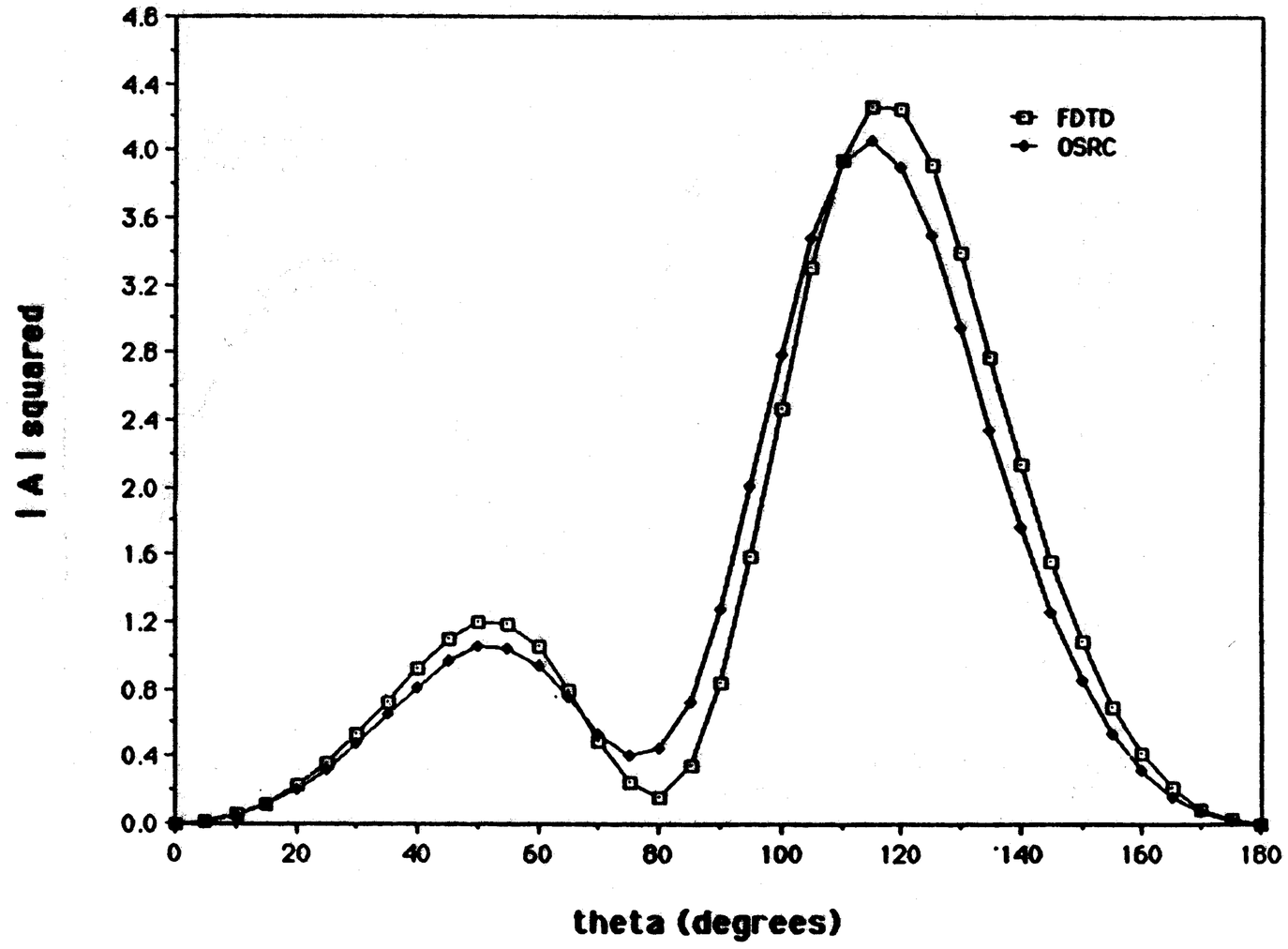

Fig. 9. Comparison of FD-TD and modal/OSRC approximate solution for bistatic radar cross section due to induced aperture field distribution of flanged open cavity [20], [31].

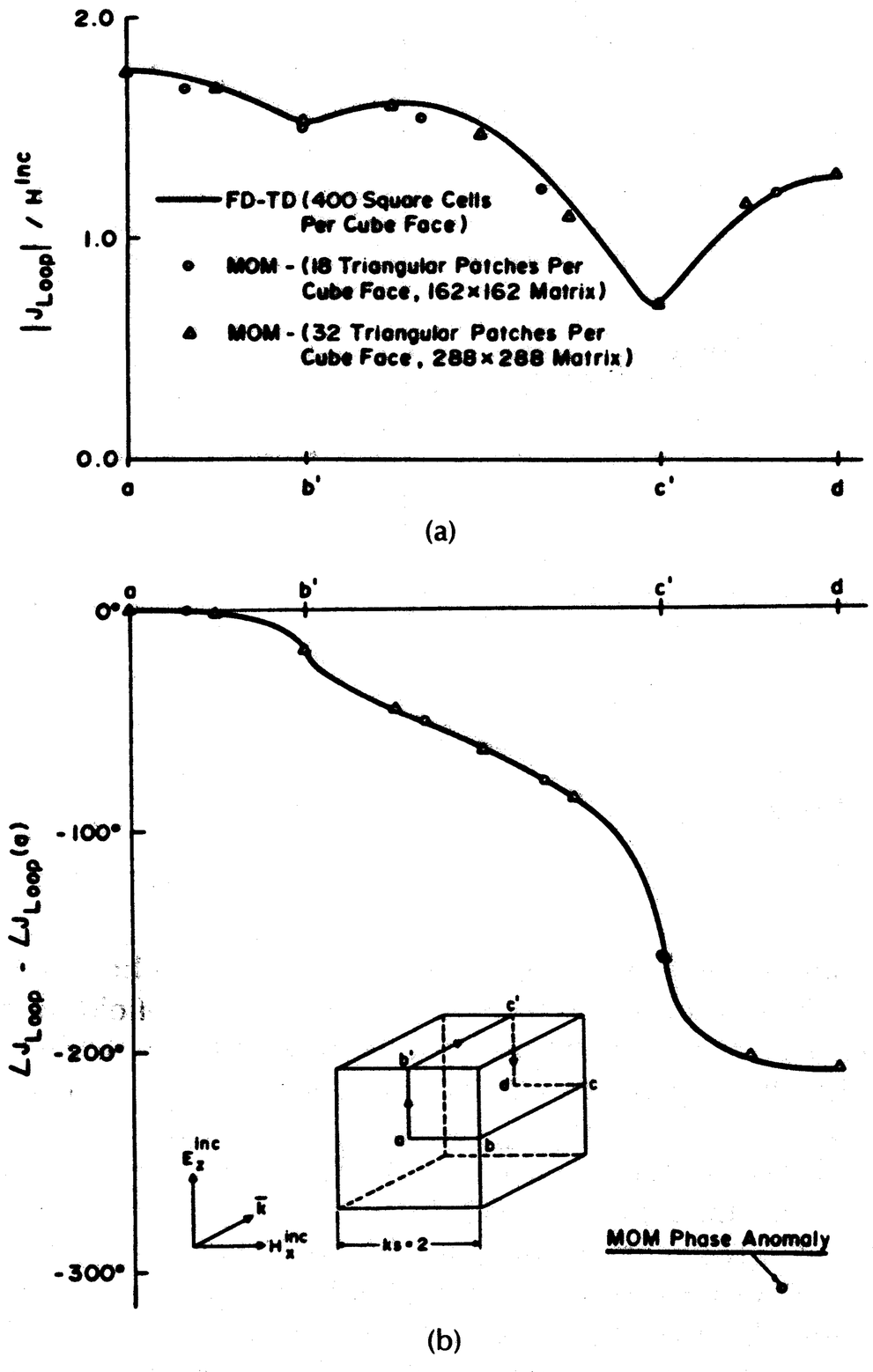

Fig. 10. Comparison of FD-TD and EFIE-MoM results for surface electric current distribution induced along *E*-plane locus of a perfectly conducting cube of size $k_0 s = 2$. (a) Magnitude. (b) Phase [13].

B. Flat Conducting Plate, Multiple Monostatic Observations [14], [24]

We next consider a 30 × 10 × 0.65 cm flat conducting plate target. At 1 GHz, where the plate spans 1 × 1/3 λ_0, a comparison is made between FD-TD and MoM results for the monostatic RCS versus observation-angle (look-angle) azimuth, keeping the elevation angle fixed at 90° as shown in Fig. 12(a). Here the FD-TD model uses a uniform cell size of 0.625 cm ($\lambda_0/48$), forming the plate by 48 × 16 × 1 cells. The radiation boundary is located at a uniform distance of *only 8 cells* from the plate surface. For the MoM model, a study of the convergence of the computed broadside RCS indicates that the plate thickness must be accounted for by using narrow side patches, and the space resolution of each patch should be finer than approximately 0.2 λ_0. As a result, the MoM model forms the plate by 10 × 3 × 1 divisions, yielding a total of 172 triangular surface patches. Fig. 12(a) shows excellent agreement between the two models, within about ±0.2 dB.

At 9 GHz, the plate spans 9 × 3 λ_0, and the use of the MoM model is virtually precluded because of its large computational burden. If we follow the convergence guidelines discussed, the plate would require appproximately 50 × 15 × 1 divisions to properly converge, yielding a total of 3260 triangular surface patches and requiring the generation and inversion of a 4890 × 4890 complex-valued system matrix. On the other hand, FD-TD remains feasible for the plate at 9 GHz. Choosing a uniform cell size of 0.3125 cm (λ_0/10.667), the plate is formed by 96 × 32 × 2 cells. With the radiation boundary again located *only 8 cells* from the plate surface, the overall lattice size is 112 × 48 × 18, containing 580 608 unknown field components (real numbers). Fig. 12(b) shows excellent agreement between the FD-TD results and measurements of the monostatic RCS versus look-angle azimuth performed in the anechoic chamber facility operated by SRI International. The observed agreement is within

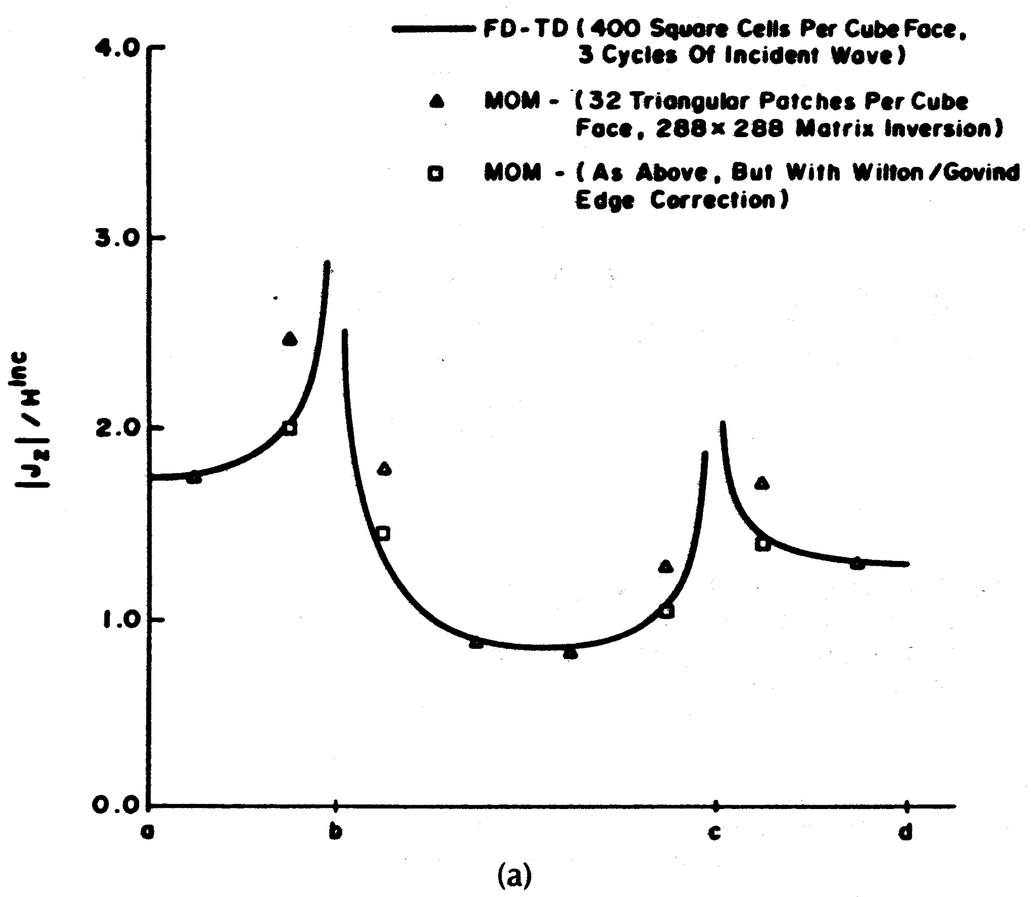

(a)

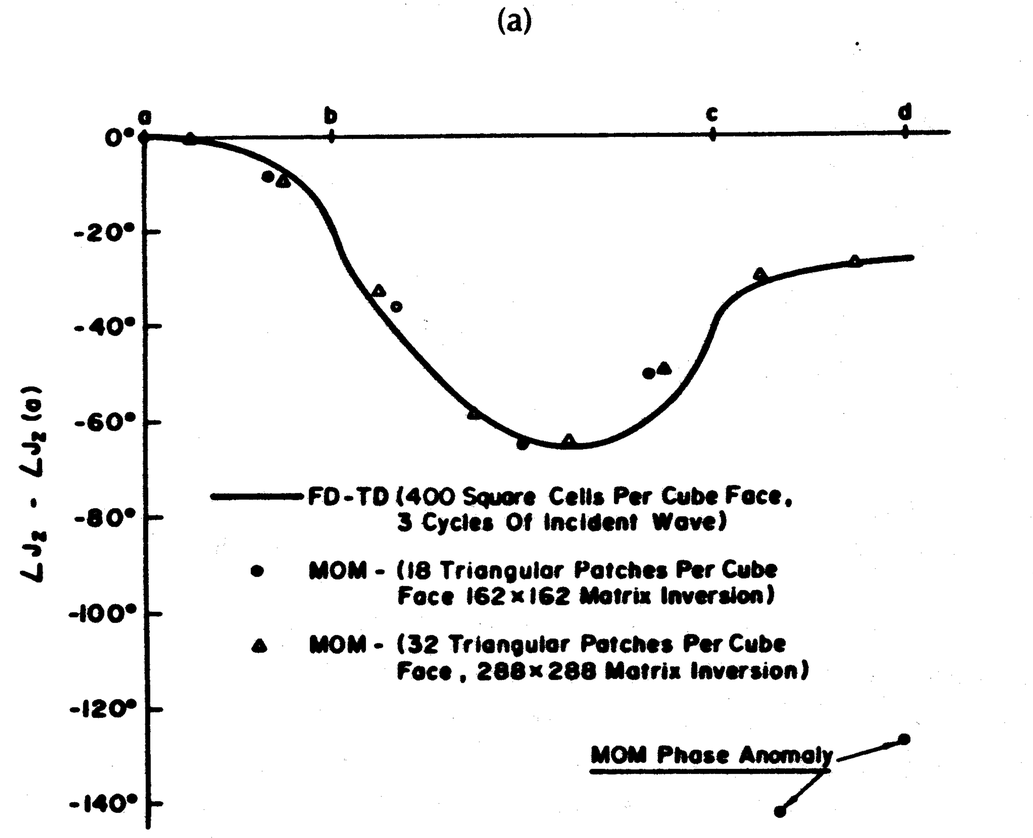

(b)

Fig. 11. Comparison of FD-TD and EFIE-MoM results for surface electric current distribution induced along *H*-plane locus of a perfectly conducting cube of size $k_0 s = 2$. (a) Magnitude. (b) Phase [13].

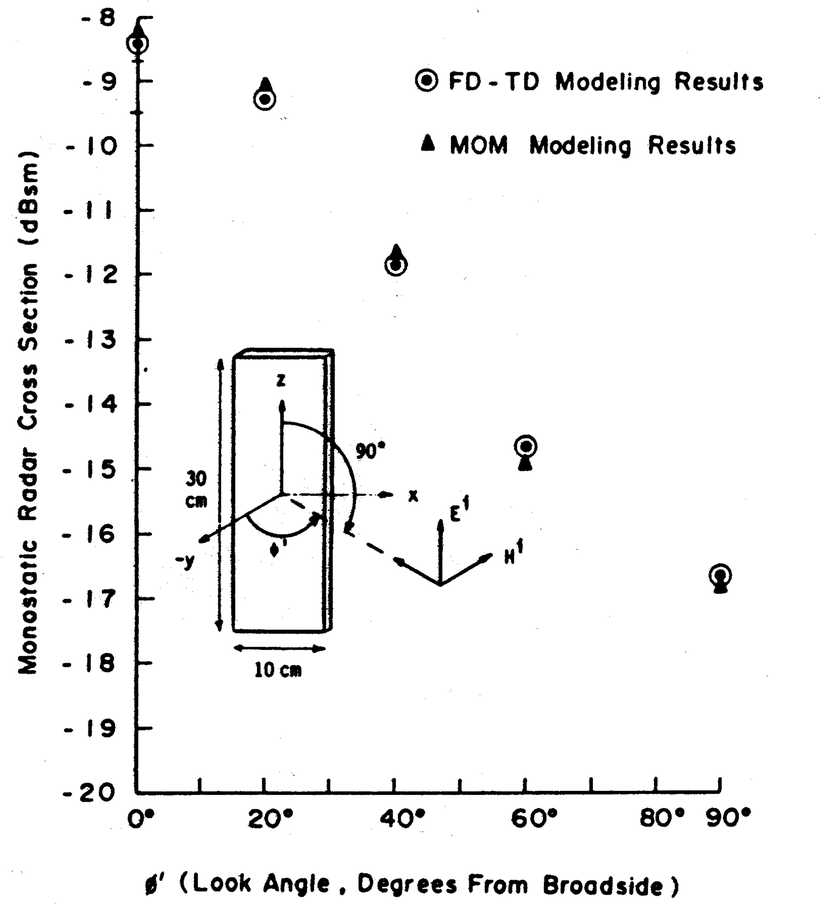

(a)

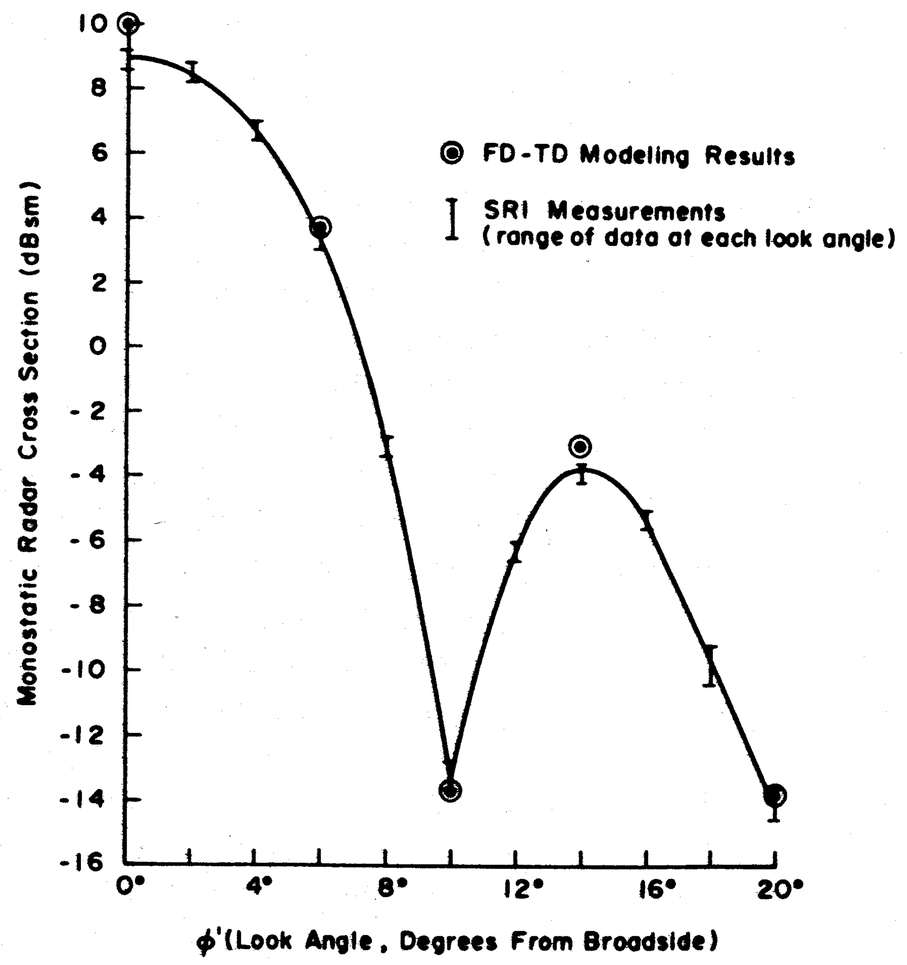

(b)

Fig. 12. Validation of FD-TD results for monostatic radar cross section of flat conducting plate. (a) Versus EFIE-MoM at 1 GHz (plate size 1 × 1/3 wavelength). (b) Versus SRI measurements at 9 GHz (plate size 9 × 3 wavelengths) [14], [24].

1 dB and 1° of look angle. As will be seen next, this level of agreement is maintained for more complicated three-dimensional targets having corner-reflector properties.

C. T-Shaped Target, Multiple Monostatic Observations [14], [24]

We last consider the monostatic RCS pattern of a crossed-plate target comprised of two flat conducting plates electrically bonded together to form the shape of a T. The main plate has the dimensions 30 × 10 × 0.33 cm and the "bisecting" fin has the dimensions 10 × 10 × 0.33 cm. (Due to a construction error, the centerline of the bisecting fin is actually positioned 0.37 cm to the right of the centerline of the main plate. This is accounted for in the FD-TD model.) The illumination is a 9.0-GHz plane wave at 90° elevation angle, polarized TE with respect to the main plate. Thus the entire T-shaped target spans 9 × 3 × 3 λ_0. Note that monostatic RCS observations at azimuth angles ϕ' between 90° and 180°, as defined in Fig. 13, are influenced by substantial corner reflector physics. This is complicated by the fact that the sides of the corner reflector have unequal lengths ($3\lambda_0$ versus $4.5\lambda_0$), and further the target is not simply a single corner reflector, but actually two corner reflectors, back to back.

For this target, the FD-TD model uses a uniform cell size of 0.3125 cm ($\lambda_0/10.667$), forming the main plate by 96 × 32 × 1 cells and the bisecting fin by 32 × 32 × 1 cells. With the radiation boundary again located *only 8 cells* from the target's maximum surface extensions, the overall lattice size is 112 × 48 × 48 cells, containing 1 548 288 unknown field components, and encompassing a total volume of 212.6 cubic wavelengths. Starting with zero-field initial conditions, 661 time steps are used per monostatic observation

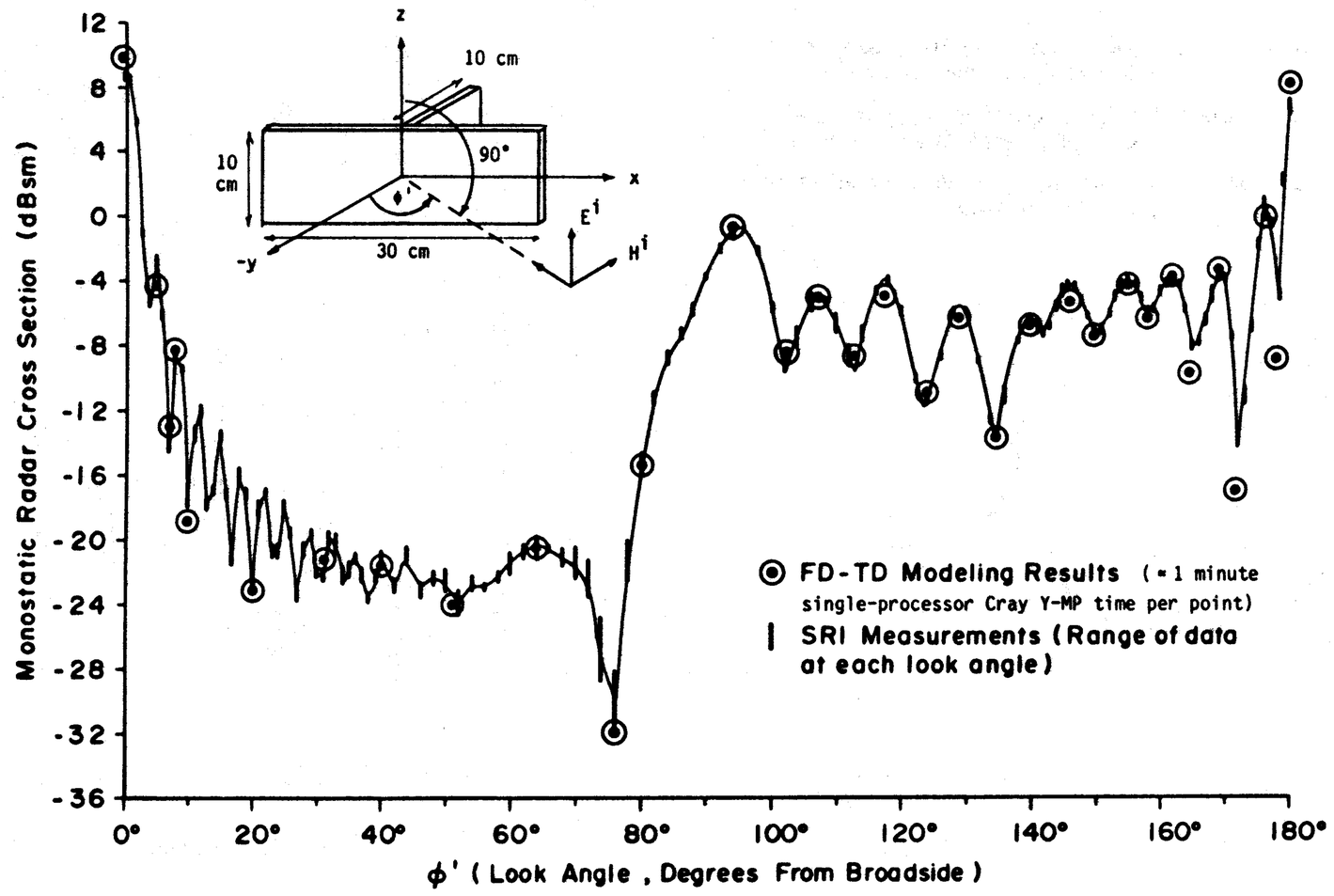

Fig. 13. Experimental validation of FD-TD modeling predictions of monostatic radar cross section versus azimuth for crossed-plate target at 9 GHz (main plate size 9 × 3 wavelengths, bisecting fin size 3 × 3 wavelengths) [14], [24].

to attain the sinusoidal steady state, equivalent to 31 cycles of the incident wave at 9.0 GHz.

Fig. 13 compares the FD-TD predicted monostatic RCS values at 32 key look-angle azimuths between 0° and 180° with measurements performed by SRI International. These azimuths are selected to define the major peaks and nulls of the monostatic RCS pattern. It is seen that the agreement is again excellent: in amplitude, within about 1 dB over a total RCS-pattern dynamic range exceeding 40 dB; and in azimuth, within 1° in locating the peaks and nulls of the RCS pattern. Note especially the fine agreement for azimuths greater than 90°, where the asymmetrical corner reflector induces an enhancement of the monostatic RCS response with substantial fine-grained detail in the RCS pattern. As of the publication of [14], this case (and similar cases studied in [24]) represented the largest detailed three-dimensional numerical scattering models of any type ever verified wherein a uniformly fine spatial resolution and the ability to treat nonmetallic composition are incorporated in the model.

VI. Potential of FD-TD for Modeling Very Complex Objects

Two characteristics of FD-TD cause it to be very promising for numerical modeling of electromagnetic wave interactions with very complex objects. 1) Dielectric and permeable media can be specified independently for each electric and magnetic field vector component in the three-dimensional volume being modeled. Since there may be tens of millions of such vector components in large FD-TD models, inhomogeneous media of enormous complexity can be specified in principle. 2) The required computer resources for this type of detailed volumetric modeling are dimensionally low, only of order N, where N is the number of space cells in the FD-TD lattice.

The emergence of supercomputers has recently permitted FD-TD to be seriously applied to a number of very complex electromagnetic wave interaction problems. Two of these are reviewed briefly.

A. UHF Penetration into a Complex Missile Seeker Section [5], [7]

Here FD-TD is applied to model the penetration of an axially incident 300-MHz plane wave into a metal-coated missile guidance section. The FD-TD model, shown in Fig. 14, contains the following elements: 1) magnesium fluoride infrared dome, 2) fiberglass nose cone and its external metal coating, 3) circular nose aperture just back of the infrared dome, 4) head coil assembly, 5) cooled detector unit with enclosing phenolic ring, 6) preamplifier can, 7) wire bundle connecting the cooled detector unit to the preamplifier can, 8) wire bundle connecting the preamplifier can to the metal backplane, 9) longitudinal metal support rods, and 10) circumferential sleeve-fitting aperture, loaded with fiberglass, where the seeker section joins the thruster. The fiberglass structure of the nose cone and its metalization are approximated in a stepped-surface manner, as is the infrared dome.

For this target, the FD-TD model uses a uniform cell size of 1/3 cm ($\lambda_0/300$), with an overall lattice size of 100 × 48 × 24 cells containing 690 000 unknown field components. (A single symmetry plane is used, giving an effective lattice size of 100 × 48 × 48.) The model, implemented on a Control Data STAR-100 (the available supercomputer at the time), was run for 1800 time steps, equivalent to 3.0 cycles of the incident wave at 300 MHz.

Fig. 15 plots contour maps of the FD-TD computed field vector components at the symmetry plane of the model. An important observation is that the wire bundles connecting the cooled detector unit, preamplifier can, and metal backplane are paralleled by high-level magnetic field contours [Fig. 15(b)]. This is indicative of substantial uniform current flow along each bundle. Such current flow would generate locally a magnetic field looping around the wire bundle

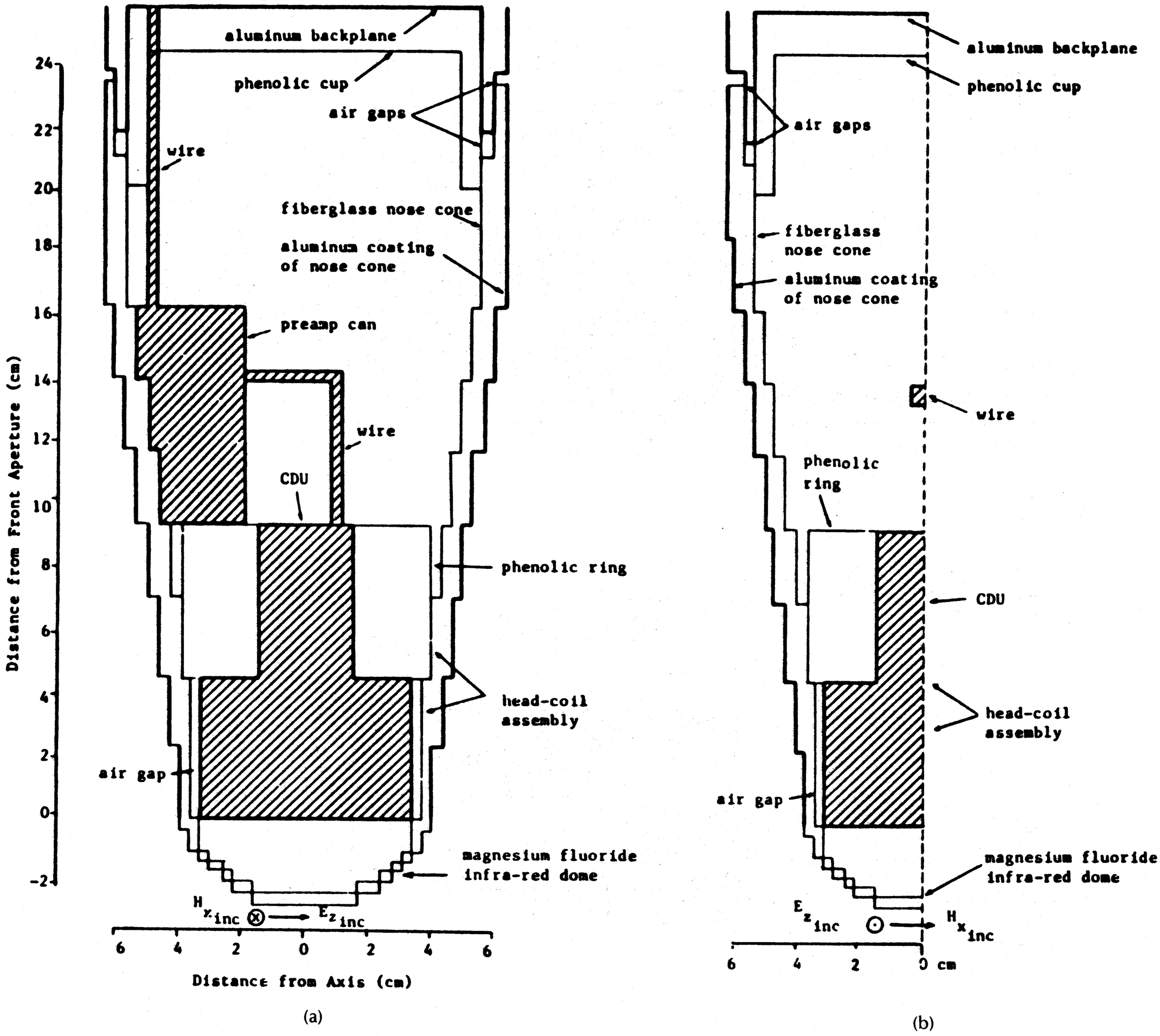

Fig. 14. Three-dimensional FD-TD model of missile seeker section showing component materials. (a) At vertical symmetry plane. (b) At horizontal observation plane [5], [7].

which, when "cut" by the symmetry plane, shows up as parallel field contours spaced equally on each side of the bundle. Using a simple Ampère's law argument, the common-mode bundle currents can be calculated, thus obtaining a key transfer function between free-field incident UHF plane-wave power density and coupled wire currents within the loaded seeker section [5]. This transfer function is useful for studies of intersystem electromagnetic compatibility and vulnerability to high-power microwaves.

Although this missile seeker model was structured to demonstrate the capability of FD-TD to map fields penetrating into a complex structure having multiple apertures and realistic internal engineering details, it should be understood that the full bistatic RCS pattern of the target is available as a "by-product" with virtually no additional effort. Further, with the 1/3-cm space resolution used, the FD-TD penetration/RCS model discussed is useful *up to 9 GHz*.

B. Whole-Body Human Dosimetry at VHF and UHF Frequencies [33], [34]

Here FD-TD is applied to model the penetration of plane waves at VHF and UHF frequencies into the entire human body. Directly exploiting the ability of FD-TD to model media inhomogeneities down to the space-cell level, highly realistic three-dimensional FD-TD tissue models of the complete body have been constructed. Specific electrical parameters are assigned to each of the electric field vector components at the 16 000 to 40 000 space cells comprising the body model. Assignments are based on detailed cross-section tissue maps of the body (as obtained via cadaver studies available in the medical literature), and cataloged measurements of tissue dielectric properties. Uniform FD-TD space resolutions as fine as 1.3 cm throughout the entire human body have proven feasible with the Cray-2 supercomputer.

Fig. 16, taken from [34], shows the FD-TD computed con-

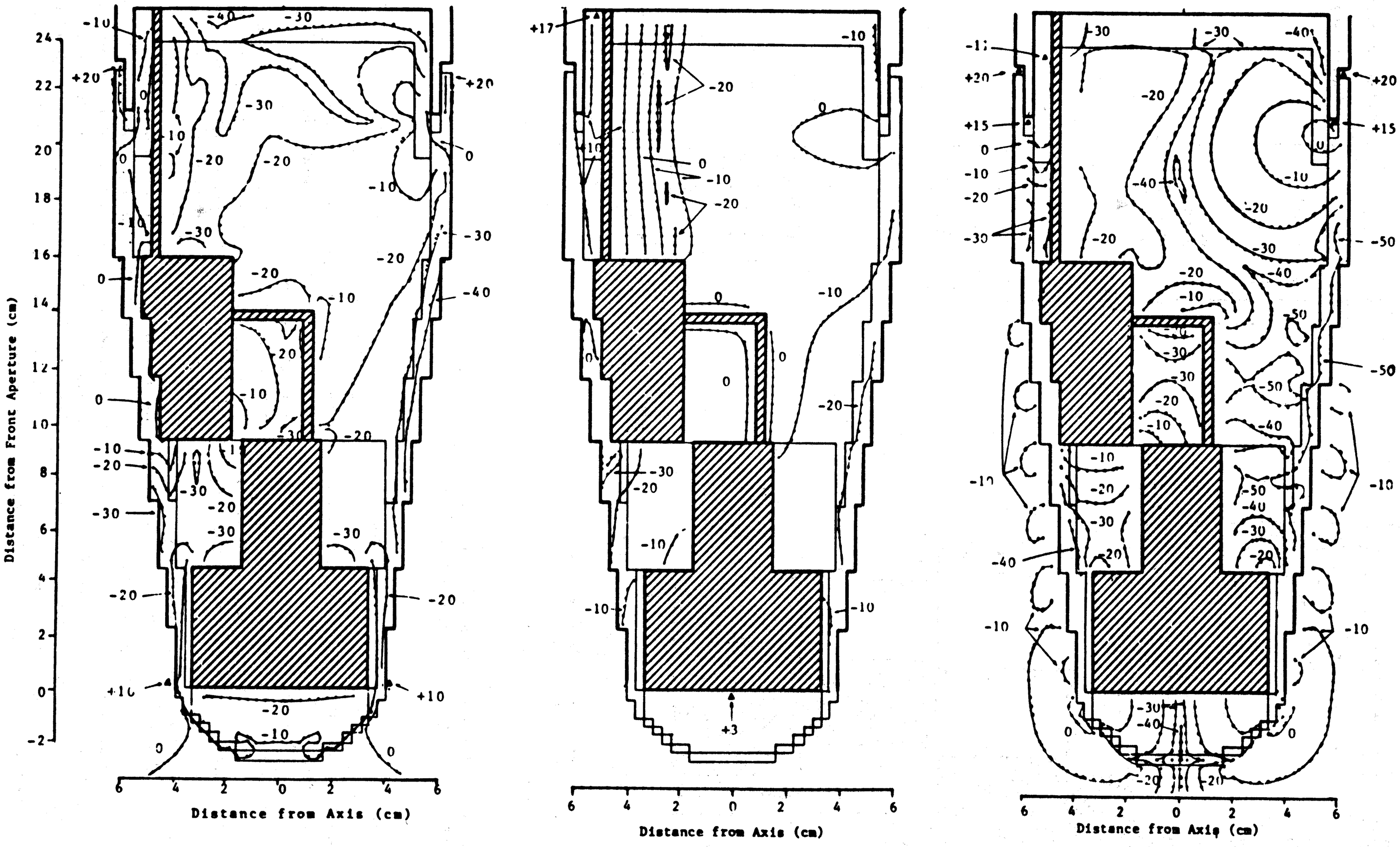

(a) (b) (c)

Fig. 15. FD-TD computed contour maps of penetrating field vector components in vertical symmetry plane of missile seeker section of Fig. 14. (a) E_z. (b) H_x. (c) E_y [5], [7].

tour maps of the specific absorption rate (SAR) distribution along horizontal cuts through the head and liver of the three-dimensional inhomogeneous human model. In Fig. 16(a) the incident wave has a power density of 1 mW/cm^2 at 350 MHz, while in Fig. 16(b) the incident wave has the same power density but is at 100 MHz. These contour maps illustrate the high level of detail of local features of the SAR distribution that is possible via FD-TD modeling for highly realistic tissue models. By implication, these results also show the applicability of FD-TD modeling to *ultracomplex* electromagnetic wave-absorbing media for RCS mitigation technology.

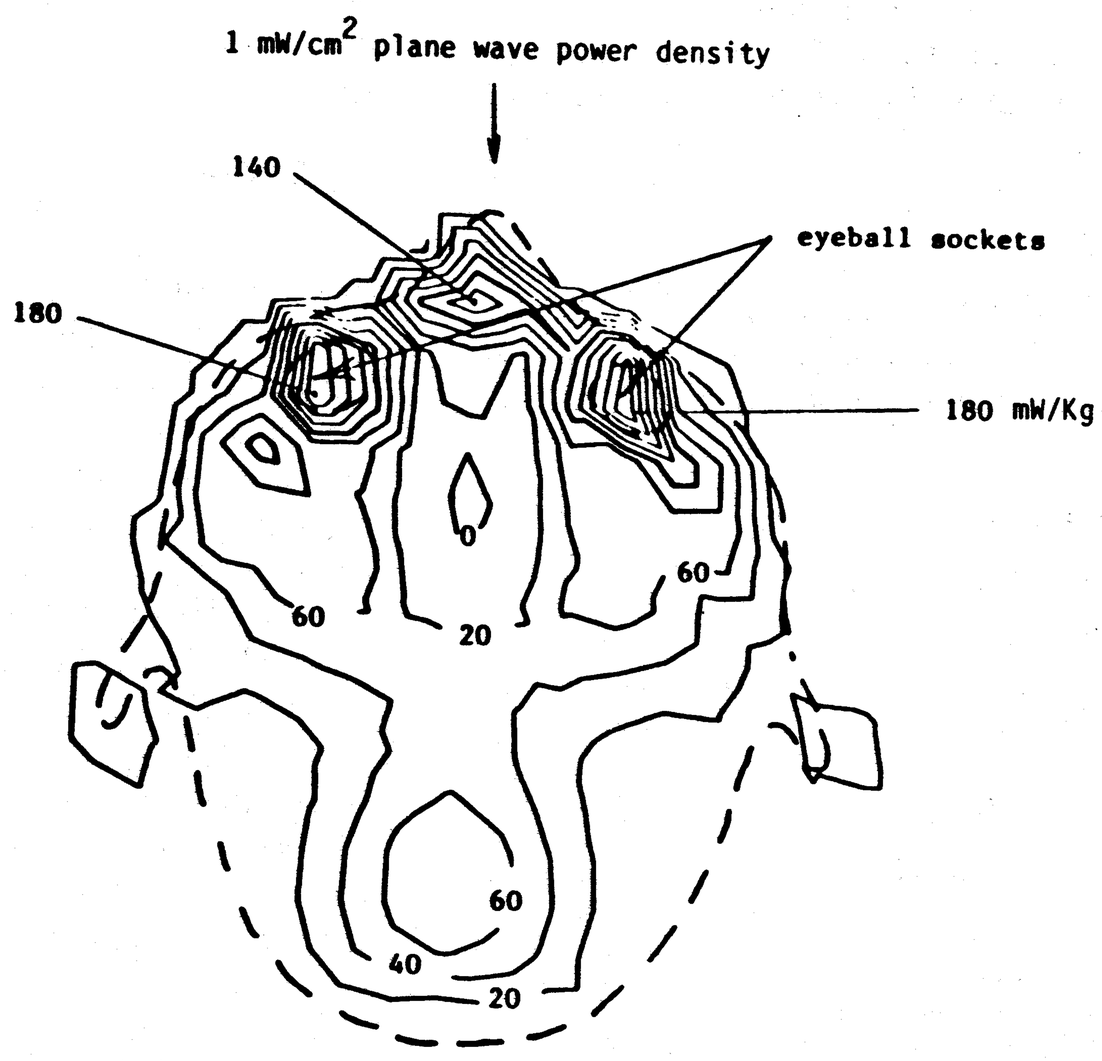

(a)

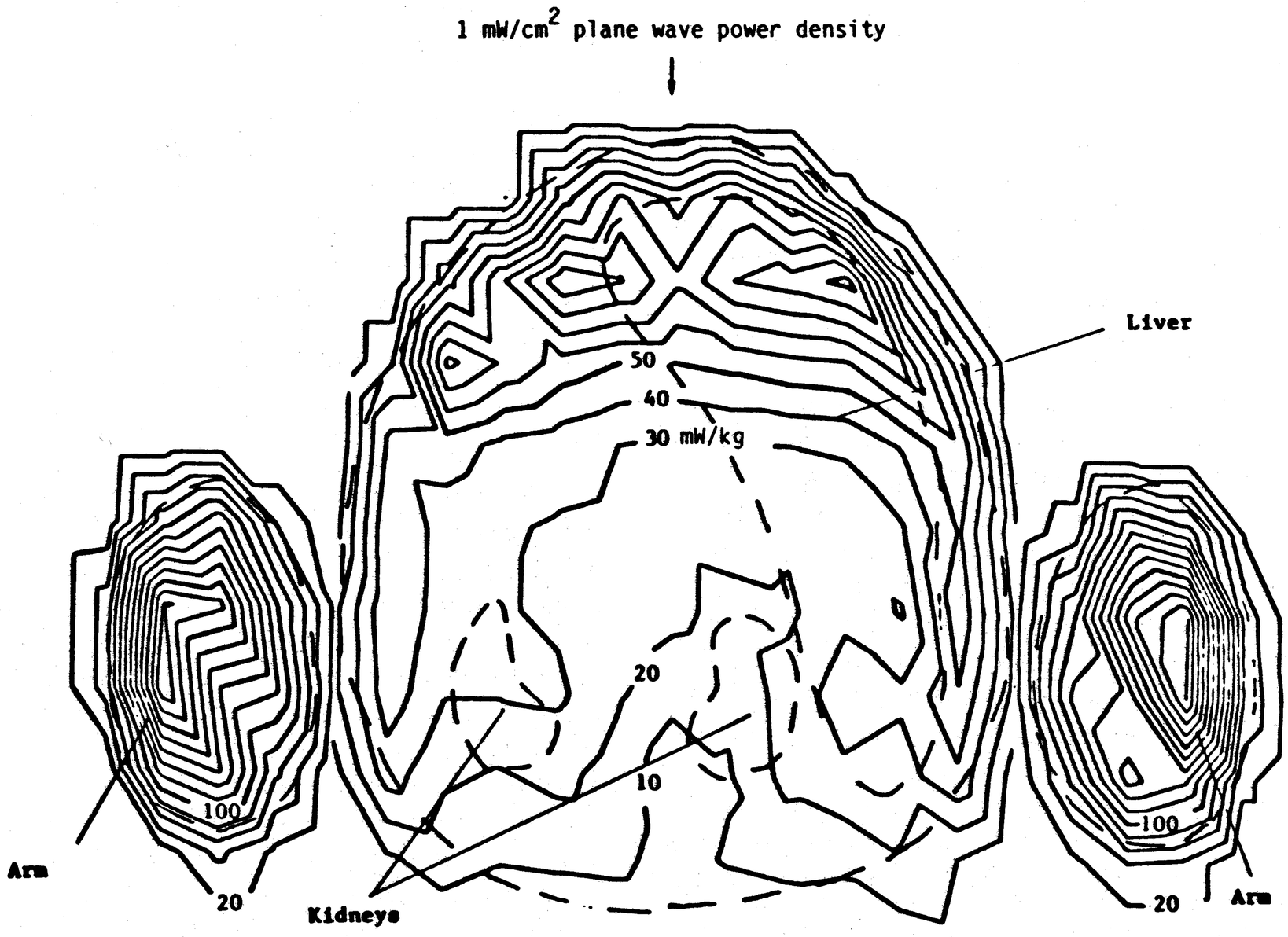

(b)

Fig. 16. FD-TD computed contour maps of specific absorption rate (SAR) due to penetrating electromagnetic fields within a highly realistic three-dimensional model of the entire human body. (a) Along horizontal cut through head at 350 MHz. (b) Along horizontal cut through liver at 100 MHz [34].

VII. Very Large-Scale Computer Software

The FD-TD method is naturally suited for large-scale processing by state-of-the-art vector supercomputers and concurrent processors. This is because essentially all of the arithmetic operations involved in a typical FD-TD run can be vectorized or cast into a highly concurrent format. Further, the order (N) demand for computer memory and clock cycles (where N is the number of lattice space cells) is dimensionally low and permits three-dimensional FD-TD models of arbitrary targets spanning 50–100 λ_0 to be anticipated in the early 1990s.

A. Cray-Based Processing

Let us now consider running times of present FD-TD codes implemented on Cray supercomputers. Table 5 lists running times for modeling one monostatic RCS observation of the $9 \times 3 \times 3$ λ_0 T-shaped target discussed in Section V-C. (Recall that this model involves an overall lattice volume of 212.6 cubic wavelengths containing 1 548 288 unknown field vector components time-stepped from zero-field initial conditions to the sinusoidal steady state over 661 time steps.) Five computing systems are listed in the table. The first is the Digital Equipment VAX 11/780 without floating-point accelerator. The second is a single processor of the Cray-2, using the VAX Fortran code either directly or after some optimization to take advantage of the vectorization and memory capabilities of the Cray-2. The third and fourth are, respectively, single-processor and eight-processor versions of the Cray Y-MP, using optimized Fortran.[2] The fifth is the 16-processor Cray-3, scheduled for initial usage in late 1989. (Running time for this case is estimated.)

Table 5 Running Times of Present FD-TD Codes for $9 \times 3 \times 3$ λ_0 T-Shaped Target

Machine	Running Time
VAX 11/780 (no floating-point accelerator)	40 hours
Cray-2 (single processor, using VAX Fortran code)	12 minutes
Cray-2 (single processor, some code optimization)	2 minutes
Cray Y-MP (single processor, optimized code)	72 seconds
Cray Y-MP (eight processors)	9 seconds
Cray-3 (sixteen processors)	3 seconds (est.)

1) 1.55-million unknown field components, 661 time steps.
2) Complete time history of the near field is computed, from zero-field initial conditions to the sinusoidal steady state.
3) Complete bistatic RCS pattern is obtained for a single illumination angle at a single frequency.
4) Running times are increased by 50–100% if an impulsive excitation with fast Fourier transform is used to obtain the bistatic RCS pattern at a multiplicity of frequencies within the spectrum of the impulsive illumination.

Table 5 reveals an extraordinary reduction of FD-TD running time per monostatic RCS observation that has occurred during the past few years. Simple extrapolation of the Cray-3 running time indicated in the table to 50-λ_0 class three-dimensional targets containing on the order of 100 000 cubic wavelengths indicates essential feasibility with no further improvements in Cray technology beyond the Cray-3. It is clear that succeeding generations of such machines in the 1990s and beyond will permit routine engineering usage of FD-TD for modeling general electromagnetic wave interactions (including RCS) involving electrically large structures.

[2]Multiprocessing on the Cray Y-MP can be trivially accomplished for this (now) relatively small target by simultaneously placing eight individual processes, each representing one monostatic observation angle, on the eight individual processors of the machine. For the much larger targets of current and future interest, this procedure will not work because of memory conflicts between processors. Such targets will require only a single FD-TD process to be run on the machine, with the computational burden for this one process shared by the available processors. Analogous statements can be made for the 16 processor Cray-3.

B. The Connection Machine

An interesting prospect that has recently arisen is the reduction of the order (N) computational burden of FD-TD to order ($N^{1/3}$). This possibility is a consequence of the appearance of the Connection Machine (CM), which has tens of thousands of simple processors and associated bit-wise memories arranged in a highly efficient manner for processor-to-processor communication. With the CM, a single processor could be assigned to store and time-step a single row of vector field components in a three-dimensional FD-TD space lattice. For example, 1 500 000 processors would be sufficient to store the six Cartesian components of E and H for each of the 500×500 rows of a cubic lattice spanning 50 λ_0 (assuming 10 cells/λ_0 resolution). FD-TD time stepping would be performed via row operations mapped onto the individual CM processors. These row operations would be performed concurrently. Thus for a fixed number of time steps, the total running time would be proportional to the time needed to perform a single row operation, which in turn would be proportional to the number of field vector components in the row, or order ($N^{1/3}$).

For the 50-λ_0 cubic lattice noted above, this would imply a dimensional reduction of the computational burden from order (500^3) to order (500), a tremendous benefit. As a result, it is conceivable that a suitably scaled CM could model one monostatic RCS observation angle of a 50-λ_0 three-dimensional target in only a few seconds, achieving effective floating-point rates on the order of 100 gigaflops (10 or more complete Cray-3s). For this reason, FD-TD algorithm development for the CM is a promising area of research for developing ultralarge numerical models of general electromagnetic wave interactions, including RCS.

VIII. Conclusion

This paper has presented a number of two- and three-dimensional examples of FD-TD numerical modeling of electromagnetic wave scattering and penetration. The objects modeled ranged in nature from simple geometric shapes to extremely complex aerospace and biological systems. In all cases studied to date where rigorous analytical, code-to-code, or experimental validations were possible, FD-TD predictive data for near fields and RCS were in excellent agreement with the benchmark data. With continuing advances in FD-TD modeling theory for target features relevant to the RCS problem, and with continuing advances in vector- and concurrent-processing supercomputer technology, it is likely that FD-TD numerical modeling will occupy an important place in RCS technology in the 1990s and beyond as the need for detailed models of three-dimensional complex material structures spanning 50 λ_0 or more becomes critical.

References

[1] K. S. Yee, "Numerical solution of initial boundary value problems involving Maxwell's equations in isotropic media," *IEEE Trans. Antennas Propagat.*, vol. AP-14, pp. 302–307, May 1966.

[2] A. Taflove and M. E. Brodwin, "Numerical solution of steady-state electromagnetic scattering problems using the time-dependent Maxwell's equations," *IEEE Trans. Microwave Theory Tech.*, vol. MTT-23, pp. 623–630, Aug. 1975.

[3] G. A. Kriegsmann, "Exploiting the limiting amplitude principle to numerically solve scattering problems," *Wave Motion*, vol. 4, pp. 371–380, 1982.

[4] A. Taflove and M. E. Brodwin, "Computation of the electromagnetic fields and induced temperatures within a model of the microwave-irradiated human eye," *IEEE Trans. Microwave Theory Tech.*, vol. MTT-23, pp. 888–896, Nov. 1975.

[5] A. Taflove and K. R. Umashankar, "Evaluation of time-domain electromagnetic coupling techniques; vol. I: Theory and numerical results," Rome Air Development Center, Griffiss AFB, NY, Final Rep. RADC-TR-80-251, Contract F30602-79-C-0039, Apr. 1980.

[6] A. Taflove, "Application of the finite-difference time-domain method to sinusoidal steady state electromagnetic penetration problems," *IEEE Trans. Electromag. Compat.*, vol. EMC-22, pp. 191–202, Aug. 1980.

[7] A. Taflove and K. R. Umashankar, "A hybrid moment method/finite-difference time-domain approach to electromagnetic coupling and aperture penetration into complex geometries," *IEEE Trans. Antennas Propagat.*, vol. AP-30, pp. 617–627, July 1982.

[8] R. Holland, "Threde: A free-field EMP coupling and scattering code," *IEEE Trans. Nuclear Sci.*, vol. NS-24, pp. 2416–2421, Dec. 1977.

[9] K. S. Kunz and K. M. Lee, "A three-dimensional finite-difference solution of the external response of an aircraft to a complex transient EM environment. Part I—The method and its implementation," *IEEE Trans. Electromag. Compat.*, vol. EMC-20, pp. 328–333, May 1978.

[10] D. E. Meriwether, R. Fisher, and F. W. Smith, "On implementing a numeric Huygen's source scheme in a finite-difference program to illuminate scattering bodies," *IEEE Trans. Nuclear Sci.*, vol. NS-27, pp. 1819–1833, Dec. 1980.

[11] G. Mur, "Absorbing boundary conditions for the finite-difference approximation of the time-domain electromagnetic field equations," *IEEE Trans. Electromag. Compat.*, vol. EMC-23, pp. 377–382, Nov. 1981.

[12] K. R. Umashankar and A. Taflove, "A novel method to analyze electromagnetic scattering of complex objects," *IEEE Trans. Electromag. Compat.*, vol. EMC-24, pp. 397–405, Nov. 1982.

[13] A. Taflove and K. R. Umashankar, "Radar cross section of general three-dimensional scatterers," *IEEE Trans. Electromag. Compat.*, vol. EMC-25, pp. 433–440, Nov. 1983.

[14] A. Taflove, K. R. Umashankar, and T. G. Jurgens, "Validation of FD-TD modeling of the radar cross section of three-dimensional structures spanning up to nine wavelengths," *IEEE Trans. Antennas Propagat.*, vol. AP-33, pp. 662–666, June 1985.

[15] B. Engquist and A. Majda, "Absorbing boundary conditions for the numerical simulation of waves," *Math. Comp.*, vol. 31, pp. 629–651, July 1977.

[16] G. A. Kriegsmann and C. Morawetz, "Solving the Helmholtz equation for exterior problems with variable index of refraction: I," *SIAM. J. Sci. Stat. Comput.*, vol. 1, pp. 371–385, Sept. 1980.

[17] A. Bayliss and E. Turkel, "Radiation boundary conditions for wave-like equations," *Commun. Pure Appl. Math.*, vol. 33, pp. 707–725, 1980.

[18] L. N. Trefethen and L. Halpern, "Well-posedness of one-way wave equations and absorbing boundary conditions," Inst. Computer Applications in Science and Engineering (ICASE), NASA Langley Research Center, Hampton, VA, Rep. 85-30, June 1985.

[19] J. G. Blaschak and G. A. Kriegsmann, "A comparative study of absorbing boundary conditions," *J. Comp. Phys.*, vol. 77, pp. 109–139, July 1988.

[20] J. G. Blaschak, "Radiation boundary conditions: I. Absorbing boundary conditions for electromagnetic wave propagation; II. Application to on-surface radiation condition analysis of canonical reentrant structures," Ph.D. dissertation, Dep. Elec. Eng. and Comput. Sci., Northwestern University, Evanston, IL, Aug. 1988.

[21] J. Fang and K. K. Mei, "A super-absorbing boundary algorithm for solving electromagnetic problems by time-domain finite-difference method," in *Proc. 1988 IEEE AP-S Int. Symp.* (Syracuse, NY, June 1988), pp. 472–475.

[22] D. T. Borup, D. M. Sullivan, and O. P. Gandhi, "Comparison of the FFT conjugate gradient method and the finite-difference time-domain method for the 2-D absorption problem," *IEEE Trans. Microwave Theory Tech.*, vol. MTT-35, pp. 383–395, Apr. 1987.

[23] B. Beker, K. R. Umashankar, and A. Taflove, "Numerical analysis and validation of the combined field surface integral equations for electromagnetic scattering by arbitrary shaped two-dimensional anisotropic objects," *IEEE Trans. Antennas Propagat.*, vol. 37, Nov. 1989 (in press).

[24] A. Taflove and K. R. Umashankar, "Analytical models for electromagnetic scattering," Electromag. Sci. Div., Rome Air Development Center, Hanscom AFB, MA, Final Rep. RADC-TR-85-87, Contract F19628-82-C-0140, May 1985.

[25] K. R. Umashankar, A. Taflove, and B. Beker, "Calculation and experimental validation of induced currents on coupled wires in an arbitrary shaped cavity," *IEEE Trans. Antennas Propagat.*, vol. AP-35, pp. 1248–1257, Nov. 1987.

[26] N. K. Madsen and R. W. Ziolkowski, "Numerical solution of Maxwell's equations in the time domain using irregular nonorthogonal grids," *Wave Motion*, vol. 10, pp. 583–596, Dec. 1988.

[27] A. Taflove, T. G. Jurgens, T. G. Moore, and K. R. Umashankar, "FD-TD conformal modeling of smoothly curved targets," submitted to *IEEE Trans. Antennas Propagat.*

[28] M. Fusco, "FD-TD algorithm in curvilinear coordinates," submitted to *IEEE Trans. Antennas Propagat.*

[29] V. Shankar and W. Hall, "A time-domain differential solver for electromagnetic scattering problems," *Proc. IEEE*, vol. 77, this issue.

[30] B. J. McCartin and J. F. DiCello, "Three-dimensional finite difference frequency domain scattering computations using the control region approximation," *IEEE Trans. Magn.*, vol. MAG-25, July 1989 (in press).

[31] J. G. Blaschak, G. A. Kriegsmann, and A. Taflove, "A study of wave interactions with flanged waveguides and cavities using the on-surface radiation condition method," *Wave Motion*, vol. 11, pp. 65–76, Mar. 1989.

[32] D. R. Wilton and S. Govind, "Incorporation of edge conditions in moment method solutions," *IEEE Trans. Antennas Propagat.*, vol. AP-25, pp. 845–850, Nov. 1977.

[33] D. M. Sullivan, D. T. Borup, and O. P. Gandhi, "Use of the finite-difference time-domain method in calculating EM absorption in human tissues," *IEEE Trans. Biomed. Eng.*, vol. BME-34, pp. 148–157, Feb. 1987.

[34] D. M. Sullivan, O. P. Gandhi, and A. Taflove, "Use of the finite-difference time-domain method in calculating EM absorption in man models," *IEEE Trans. Biomed. Eng.*, vol. 35, pp. 179–186, Mar. 1988.

Allen Taflove (Senior Member, IEEE) was born in Chicago, IL, on June 14, 1949. He received the B.S. (with highest distinction), M.S., and Ph.D. degrees in electrical engineering from Northwestern University, Evanston, IL, in 1971, 1972, and 1975, respectively.

From 1975 to 1984 he was a staff member in the Electronics Division, IIT Research Institute, Chicago, IL, holding the positions of Associate Engineer, Research Engineer, and Senior Engineer. During this time, he was principal investigator on a number of externally funded research programs, including five that contributed to the early development of the finite-difference time-domain (FD-TD) method for computational modeling of electromagnetic wave interactions with complex structures. He was also a key contributor to large-scale programs involving the

application of radio-frequency heating to produce oil in place (without mining) from deposits of oil shale, tar sand, and heavy oil; to accelerate oil production from slowly producing conventional wells; and to decontaminate large sections of the ground permeated with toxic chemical wastes. In this technical area, he has been awarded 10 U.S. patents to date. In 1984, he returned to Northwestern University where he is currently Professor of Electrical Engineering and Computer Science. He is actively pursuing large-scale computational modeling of linear and nonlinear electromagnetic wave phenomena. Additional research interests include inverse scattering/target synthesis, the new on-surface radiation condition (OSRC) theory, computational optics, and applications of the most recent vector and concurrent supercomputers to large-scale electromagnetic modeling.

Dr. Taflove is a member of Tau Beta Pi, Eta Kappa Nu, Sigma Xi, and Commission B of URSI. He is coauthor of the Best Paper at the 1983 IEEE International EMC Symposium, Washington, DC.

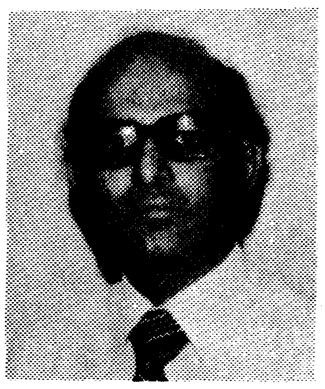

Korada Umashankar (Senior Member, IEEE) received the B.E. degree from Mysore University, India, in 1962, the M.E. degree from the Indian Institute of Science, Bangalore, in 1964, and the Ph.D. degree from the Indian Institute of Science, Bangalore, in 1964, and the Ph.D. degree from the University of Mississippi, University, in 1974, all in electrical engineering.

From 1964 to 1969 he was Assistant Professor and Head of the Department of Electrical Engineering, College of Engineering, Karnatak University, Hubli, India. During 1974–1975 he was a Post-Doctoral Research Associate, and during 1975–1977 Assistant Professor of Electrical Engineering at the University of Mississippi. From 1977 to 1979 he was a National Research Council Visiting Fellow at the Air Force Weapons Laboratory, Kirtland AFB, NM, involved with simulator studies and electromagnetic transients. From 1979 to 1984 he was Senior Engineer in the Electronics Division, IIT Research Institute, Chicago, IL, involved with the development of numerical models for electromagnetic interaction with complex objects. At present he is Associate Professor of Electrical Engineering, University of Illinois at Chicago, Chicago. His primary research work has been in the development of analytical and mathematical techniques in electromagnetic theory, EMP/EMC interaction, and EM simulation studies.

Dr. Umashankar is a member of Sigma Xi, Eta Kappa Nu, AAAS, and Commission B of URSI.